Designing a Shack-Hartmann based wavefront sensor for eye aberrometry

Master's thesis
University of Turku
Physics
2025
B.Sc. Joska Tommola
Examiners:
PhD Kari Vienola
Dos. Matti Murtomaa

The originality of this thesis has been checked in accordance with the University of Turku quality assurance system using Turnitin Originality Check service.

UNIVERSITY OF TURKU
Department of Physics and Astronomy

Tommola, Joska Designing a Shack-Hartmann based wavefront sensor for eye aberrometry

Master's thesis, 79 pp.
Physics
August 2025

The focus of this thesis was to design and build a low-cost SH-WFS based imaging device to do ocular aberrometry. One of the most remarkable disadvantages of building your own Shack-Hartmann Wavefront Sensor (SHWFS) is the costs, and this study tries to find out if it is possible to use cheaper components and get reliable results. In addition to off-the-shelf components, 3D modeling and printing is utilized to design custom components for the system.

The measurements of aberrations are closely related to the wavefronts. The wavefront is the shape of a light wave, and every point of it has the same phase. If the measured wavefront deviates from the reference it means the presence of aberration which are determinated as Zernike polynomials. SHWFS is used as a sensor to measure the locations of light spots, and this plays a crucial role in determining aberrations because aberrations are based on the displacements of light spots from reference positions. SH-WFS was chosen for wavefront detection due to its simplicity and broad use in ophthalmology and astronomy.

Before building the optical system, several different parameters had to be calculated, such as the optimal wavelength of the imaging beam, the used optical power and diameter of the beam entering the eye. The parameters create a background for the building, analysis and measurements of the aberrometer. Besides all these parameters, the functionality of individual components was tested (light source, neutral density filters, trial lenses and imaging sensor).

The theory and the experimental results are in good agreement. The spot size in the measurements was 39.94-41.14 µm and theoretical calculation was 40.4 µm. The size of the spot means the diameter of the spot in the lenslet. The quality of the spots was also good because the single spots were well fitted by Gaussian functions. The best signal-to-noise ratio was applied with an exposure time of 2.5 ms. Wavefront maps showed logically increasing defocus aberration with negative trial lenses. The positive trial lenses gave unreliable results, and it is probably due to the inappropriate trial lens holder for them. The work presented in this thesis shows that it is possible to construct a low-cost aberrometer with off-the-shelf components and obtained results have laid the groundwork for future development of the device.

Keywords: wavefront sensing, Shack-Hartmann wavefront sensor, aberrometry, eye

Contents

1 Introduction

A wavefront describes the surface of light, which means that the light wave has the same phase at every point. The wavefront is a two-dimensional space. In the ideal case, the wavefront is just a straight line. The wavefront measurement is based on the reference measurement, which should be as flat as possible [1]. However, there are some small aberrations in the measurements that weaken the reliability of the measurements. The reference measurement is compared to real measurement and aberration is calculated according to the differences between these. Possible reasons for aberrations are, for example, eye, imperfect collimation and dispersion of the material, which means that the refractive index depends on the wavelength of the light.

Wavefront sensing (WFS) plays a significant role in optics because it gives information about optical imperfections and makes it possible to fix them. For example, wavefront measurement is used in eye imaging and astronomy. The most common way to do it is to use Shack-Hartman wavefront sensing (SHWFS). SHWFS is based on the microlens array (MLA) and Complementary Metal-Oxide-Semiconductor (CMOS) or charge-coupled device (CCD) camera [2]. The MLA includes many small areas, called lenslets, that focus the light in the CMOS or CCD camera [3]. The aberrations can be calculated from the shifts of the light spots.

Aberrations are closely related to wavefront sensing because aberrations mean that wavefronts deviate from the ideal wavefront [4]. In practice, this means that the wavefront is not flat anymore. These aberrations are measured with the help of SHWFS or other sensors, such as a pyramid sensor or a shearing interferometer [5, 6]. The principle of measuring aberrations of the eye is based on reflection. The incoming light to the eye hits the retina and the reflected light from the retina is measured as a wavefront in the SHWFS.

As WFS is able to detect ocular aberrations, it is a crucial component in adap-

tive optics (AO). The key idea of AO in retinal imaging is that the WFS detects aberrations and corrects for them using a deformable mirror (DM). They work together in a closed loop to make the wavefront as flat as possible, which improves the imaging resolution. Overall, AO consists of three different parts, the WFS being the first part. After that, the data are transferred to the control computer, which converts the raw data into voltages. The voltages are sent to the wavefront corrector, which creates a conjugate surface shape to the wavefront [7]. Although SFWFS can work as a stand alone unit, it is often built into the imaging system. Many research groups build their own SHWFS because it is relatively easy. In SHWFS, many different sensors and microlens solutions can be used. The disadvantage of building the own SHWFS is the expenses and thus it is also beyond the reach of many research groups.

The purpose of this study is to build an aberrometer to measure aberrations of the eye. To keep the system low-cost, majority of the components are off-the-shelf, resourced from well-known optical component distributors. The custom components are designed in-house using Fusion 360 and manufactured with 3D-printing. To test the feasibility of the system, model eye is imaged and known aberrations are introduced to the optical path to see how they are measured. The measurement protocol consists of two different parts. In the first part, model eyes are imaged and in the second part, trial lenses are imaged.

2 Eye

Vision is one of the most critical human senses which allows us to observe the world around us. The human eye is sensitive to light within the 400-700 nm wavelength range. This range includes colors from violet (400 nm) to red (700 nm). The image captured by the eye is initially formed upside down, but the brain processes and interprets it right-side up. The human eye consists of various components that play

a vital role in capturing and processing visual information. Figure 1 illustrates the key structures of the eye. This chapter explores the anatomy of the eye, its optical properties, and some of the most common vision disturbances, providing insight into how these factors affect visual perception.

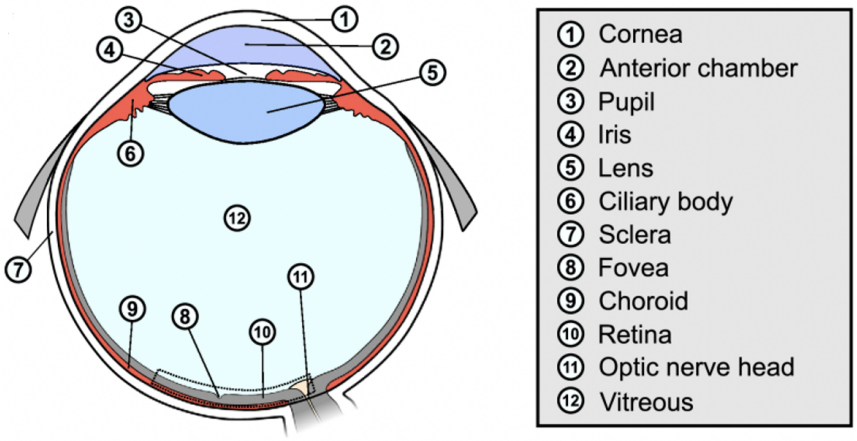

Figure 1: The key components of the eye. Light travels through the cornea (1), pupil (3), and lens (5) of the eye, continues through the vitreous body (12), and finally reaches the retina (10), where the rays converge and the image is formed. The optic nerve (11) then transfers this information to the brain [8].

2.1 Anatomy of the eye

This chapter describes the different parts of the eye: cornea, pupil, iris, lens, vitreous body, retina, and choroid. The eye is a complex organ, and in this context, only the parts that affect how light travels through it are considered. The cornea and the lens affect the most to the refraction of the light, as seen later in Chapter 2.2.

Cornea

The cornea is located on the surface of the eye and serves several critical functions. One of its most important functions is to protect the eye, while also significantly influencing how light rays are focused onto the retina. The mean thickness of the

cornea is between 540-550 µm [9, 10] and the thickness of the cornea also tends to decrease with age [11].

The cornea consists of many different layers. The front layer of the cornea is a tear film which is 4-7 µm thick and it is composed of three different layers: aqueous, mucous and oily layers. The tear film plays an important role because it moistens the cornea and keeps the surface smooth [12, p. 15]. The second outer layer is the corneal epithelium. This epithelium consists of five or six distinct layers, including superficial cells, wing cells, and columnar basal cells. The third and largest is stroma, which comprises approximately 90% of the corneal area. Many physical properties of the cornea, for example, transparency and physical strength, are due to stroma [13, p. 10]. Between the stroma and the innermost layer, the endothelium, lies the Descemet membrane. Descemet's membrane is quite thick and transparent. This membrane anchors the endothelium to the cornea and also allows nutrients to enter the stroma [14].

Pupil and Iris

Light passes through the pupil and the iris before reaching the lens. The primary function of the iris and pupil is to regulate the amount of incoming light. The normal pupil size is approximately 4.2 mm [15] and there are many different factors that affect the size of the pupil. Luminance has the largest influence on size; higher levels of brightness cause the pupil to constrict, while lower light levels cause dilation. Focusing the vision on a nearby object also makes the pupil constrict. The second significant factor is age because older people tend to have smaller pupil sizes [16]. The pupil can also dilute due to increased levels of arousal or mental effort [17]. In addition, drugs can have an impact on the size of the pupil. Some drugs can cause dilation, called mydriatics. These act by stimulating sympathetic division or blocking its parasymphatetic division. Drugs can also cause constriction, called

miotics, by acting in a converse way compared to mydriatics [12, p. 49]. Furthermore, myopes also have larger pupilles than hyperopes [16]. The size of the pupil also plays an important role in medicine because doctors may examine the pupil with a flashlight due to suspected brain damage [18].

There are two different muscles that regulate constriction and dilation. The iris sphincter muscle, that encircles the pupil, is controlled by the parasympathetic nervous system. Dilation is controlled with the help of the iris dilator muscle. On the contrary, this muscle is controlled by the sympathetic nervous system [17].

Lens

The lens is located behind the pupil and iris within the cavity of the eyeball [19]. The lens consists of four different parts: zonules, lens fiber, lens epithelium, and lens capsule. Zonules are an important structure because the lens is attached to the ciliary muscle by them [20]. The lens thickness is estimated to be 3.6 mm in the unaccommodated state for a young eye [12, p. 29].

The primary function of the lens is to focus light onto the retina. The lens allows wavelengths ranging from 390 nm to 1200 nm to pass through. Although human visual perception is limited to around 720 nm, the lens also transmits infrared light due to its wider wavelength range [21].Aging also has an affection for the lens, and the consequence is that the lens becomes increasingly yellow with age. This means that the observation of blue light is weakened [22]. The transparency of the lens also decreases with age and causes cataract, which is the most common reason for blindness globally [23].

In an unaccommodated form, when the focus is far, the lens is flattened because the ciliary muscles pull the lens. In case of near vision, the ciliary muscles are relaxed and the lens becomes rounder in shape, increasing the thickness of the lens [12, p. 26]. The ciliary muscles are responsible for the accommodation which refers

to the process of changing the shape of the lens to adjust the focusing ability of the eye. This alters the refractive power of the lens [24].

Vitreous body

The vitreous body consists of a vitreous gel that is primarily composed of water (approximately 98%). In addition to water, the vitreous body contains glycosaminoglycans, collagens, and noncollagenous structural proteins. The gel structure is maintained with thin and unbranched collagen fibrils. The vitreous body occupies approximately 4.5 ml, forming a spherical structure surrounded by the pars plana, the retina, and the lens [25].

The vitreous body has many important functions. It contributes to oxygen metabolism and cellurar barriers and refraction. The vitreous gel is also important to maintain elasticity and reduce scattering [26]. However, if the vitreous body has opacity, it can cause scattering. This may cause interference in vision. The reason for this is vitreous floaters, which can significantly weaken the quality of life. In addition, vitreous floaters are not considered a disease due to insufficient scientific information on how this condition should be determined [27].

Retina and choroid

The retina consists of the pigmented and the neural layer. The pigmented layer contains epithelial cells that contain melanin. The neural layer consists of the ganglion cell layer, the bipolar cell layer and the photoreceptor layer. The layers of ganglion and bipolar cells let light pass through. Instead of letting light through, the photoreceptor layer converts the light into nerve impulses. This is carried out with the help of cones and rods. The cones are responsible for color vision, with approximately 6 million in the retina, while 100 million rods enable vision in low-light conditions [19]. The cones are located in the fovea, a small pit-like region of the retina that

is specialized for high-acuity vision [28]. Cones and rods play an important role in phototransduction where light is converted into electrical signal.

Figure 2 describes how the signal is converted into the optic nerve. Incoming light passes through the ganglion cells and bipolar cells and then hits the photoreceptors. Rods and cones are located in the photoreceptor and convert this light into nerve impulses. After that, the nerve impulses travel through bipolar and ganglion cells.

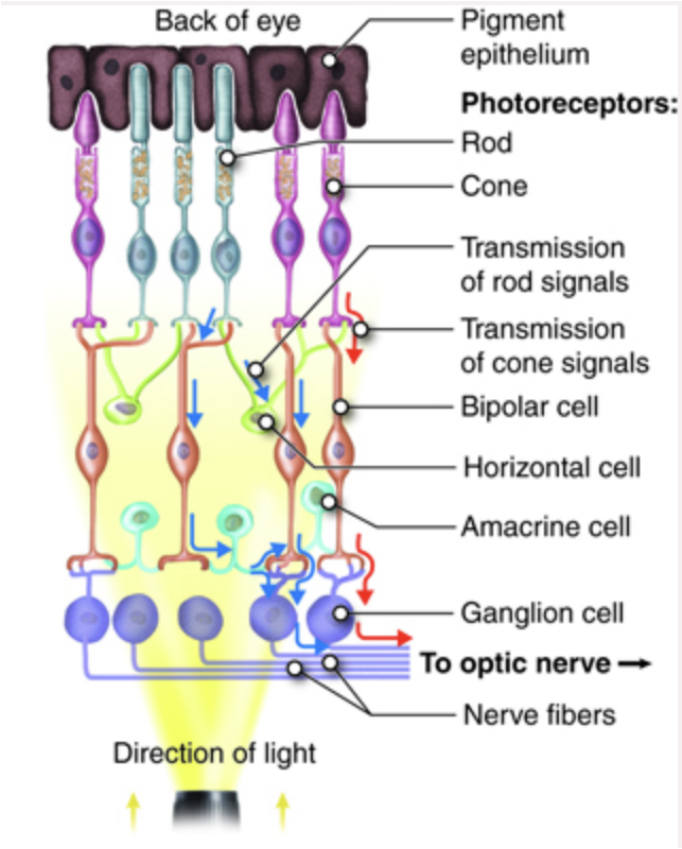

Figure 2: The light goes through the ganglion cells and bipolar cells and it hits to the photoreceptors. Rods and cones convert the light into nerve impulses through bipolar cells and ganglion cells to the optic nerve [29].

The choroid is located between the retina and the sclera, performing three important tasks. First, melanocytes within the choroid produce melanin, which absorbs excess light, reducing reflection and scattering. The second task is carried out with blood vessels by bringing nutrients to the retina [19]. The third task is to regu-

late the ocular temperature. There is also evidence that choroids participate in the growth of the eye, which can influence myopia [30].

2.2 Optics of the eye

The cornea has a significant refractive power for the eye, and it actually contributes two-thirds of the refractive power. The refractive index of the cornea is 1.376 [13, p. 4]. The dioptre value of the whole eye is 60D, but it varies depending on the eye. We can also calculate the corneal power with the help of Equation 1.

$$F = \frac{(n' - n)}{R}, \tag{1}$$

where F is the corneal power, n' is the refractive index of the internal surface, n is the refractive index of the external surface and R is the radius of anterior or posterior curvature [12, p. 17]. The total value of corneal power can be estimated as the sum of the anterior and posterior surface powers, which is approximately 42 D.

The anterior chamber locates behind the cornea and contains aqueous humor. The aqueous humor consists mostly of water, so its refractive index is 1.336, almost equal to that of water. The difference in refractive power is quite small between the cornea and the aqueos humor, so the light bends only slightly in the aqueos humor [31, p. 420].

Following the aqueous humor, the next refractive component is the lens. The lens is controlled by the ciliary muscle and it also affects refraction. When the ciliary muscles are relaxed, the lens becomes curved and the refraction power is increased. In contrast, when the ciliary muscles are tensed, the refraction power decreases. The refractive index is the largest in the middle of the lens, 1.41, and in the periphery, it is only 1.38. The lens power ranges from 19 to 22 D [12, p. 29-31]. Equation 2 determines the value of the refractive index in different locations of the lens

$$n(r) = n_0 + (n_s - n_0)r^{2p}, \tag{2}$$

where $n(r)$ is the relative distance in any direction, n_0 is the highest refractive index and n_s is the refractive index on the lens surface and p describes the steepness of the gradient [32]. The vitreous humor is the final part of the eye before the retina. Its refractive index is 1.337, so it does not have a great impact on the refraction of light [31].

2.3 Refractive errors

People may experience visual impairments or refractive errors. These conditions can include myopia (nearsightedness), hyperopia (farsightedness), astigmatism and presbyopia (age-related difficulty focusing on near objects). Such impairments occur when the eye's optical system fails to properly focus light onto the retina, leading to blurry vision at certain distances. They are correctable with glasses, contact lenses, or refractive surgery.

Refractive errors mathematically

The refractive errors are measured as diopters, which describes the optical refraction. The diopter is the inverse of the focal length as shown in Equation 3

$$D = \frac{1}{f}, \tag{3}$$

where D is the diopter and f if the focal length of the lens. The unit of diopter is m^{-1}. The spherical aberration (SE) value is a value that can be used as a definition for different refractive errors. Equation 4 includes two different parameters for SE calculation

$$SE = S + \frac{C}{2}, \tag{4}$$

where parameter S describes the spherical component, indicating possible myopia or hyperopia, and C describes the cylindrical component, indicating possible astigmatism [33].

Emmetropia

Emmetropia refers to the condition in which the light is accurately focused onto the retina by the eye's optical system. This means that the refractive power of the cornea and lens is in balance with the axial length of the eye [34]. Thus, emmetropia means normal vision ability. The eye is determined as an emmetropic if the value of the diopter is between -0.5 D and 0.5 D [35]. The example of this condition is shown in Figure 3.

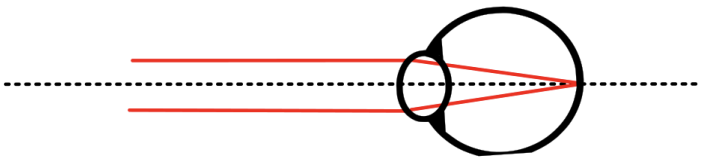

Figure 3: This shows how the light rays are focused perfectly in the retina. The consequence is that the image is possible to be clear and sharp.

Myopia

Myopia refers to a condition in which light is focused in the front of the retina. As a consequence, distant objects appear out of focus and blurry, while nearby objects remain clear. Myopia can be fixed with divergent lenses (minus lenses), which have a negative dioptric power. Myopia is typically caused by the eyeball being too long in relation to its refractive power [34]. The severity of myopia is determined according

to the negative diopter value (D). It is low if 0>D>-0.5, moderate when -3<D<-0.5 and high when D<-3 [35].

There risk factors for myopia are near work, higher educational level, less time spent outdoors and a parental history of myopia. The prevalence of myopia is highest in Asia, especially in China, and in the urban environment [36]. According to the World Health Organization, myopia affected 22% of people in 2000, but in 2050, it is estimated to influence 52% of people [37]. Myopia is also described in Figure 4.

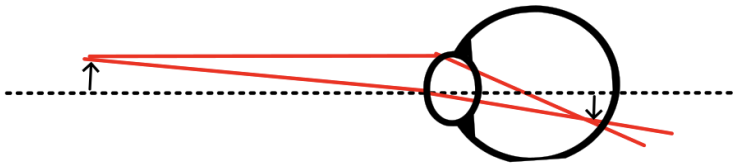

Figure 4: It can be clearly seen that the focused point is formed in the front of retina, which defines the condition known as myopia. Red lines describe the refraction of the light and the right arrow indicates the location where the image is formed.

Hyperopia

Hyperopia occurs when the image is formed behind the retina, as illustrated in Figure 5. As a result, nearby objects appear out of focus and blurry, while distant objects remain clear. This can be corrected using converging lenses (plus lenses) that compensate for the insufficient refractive power of the eye. Hyperopia is typically caused by the eyeball being too short in relation to its refractive power [34]. Hyperopia is expressed as a positive diopter value. Hyperopia is low when 0<D<+0.5, moderate between +0.5 and +3 and high when D>+3 [35].

Babies are often hyperopic, but hyperopia decreases in early childhood [38]. In general, hyperopia is more common in young people. The prevalence of hyperopia is 8.4 % at six years of age, 2-3 % between 9-14 years of age, and 1.5 % at age 15

[39]. 40 studies were compared in the calculation of these percents.

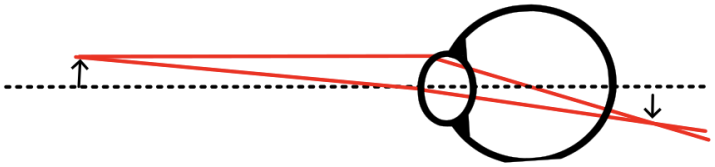

Figure 5: It can be clearly observed that the focused point is formed behind the retina and the definition for that is hyperopia. Red lines describes the refraction of the light, while the arrow indication the location where image is formed.

Astigmatism

Astigmatism means that the eye cannot form a point image of the point object because the refractive index is not consistent in all meridians. This leads to astigmatism [40]. The prevalence of astigmatism is estimated to be about 10-13 % of all refractive errors. Figure 6 shows that the focal points are not focused in the same places due to the different refractive index.

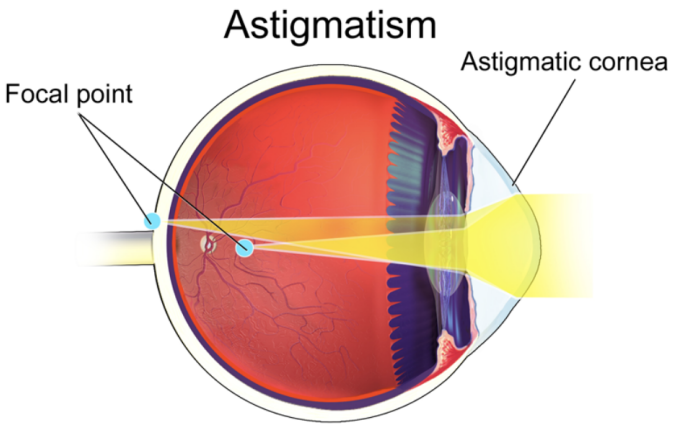

Figure 6: In astigmatism, the different meridians don't have similar refractive index. As seen in this figure, the focal point is formed in different locations [41].

Astigmatism can be classified in several ways and a common division is corneal, lenticular and total. Lenticular astigmatism refers to astigmatism caused by the lens

and total astigmatism refers to the combination of corneal and lenticular astigmatism [42].

The second possible way to classify astigmatism is to categorize it into three types based on the orientation of the principal meridians, which are perpendicular to each other. The three types are with-the-rule astigmatism, against-the-rule astigmatism and oblique astigmatism. The vertical meridian has the steepest curve in with-the-rule astigmatism, whereas the horizontal meridian has the steepest curve in against-the-rule astigmatism. Oblique astigmatism refers to a condition in which the steepest curvature of the cornea is oriented at an angle that falls between 120° and 150° or between 30° and 60° relative to the horizontal axis [43].

The third possible way to classify astigmatism into myopic, hyperopic and mixed astigmatism. Myopic astigmatism means that both astigmatism and myopia are present in the eye, similarly hyperopic astigmatism means that hyperopia and astigmatism are present. Mixed astigmatism means that part of the astigmatism is myopic and another part is hyperopic [35].

Astigmatism is measured as dioptres. It is often classified as a mild (<1.5 D), moderate (from 1.5 D to 2.0 D) and severe (>2.0 D) [44]. Myopic astigmatism, hyperopic astigmatism and mixed astigmastism can be calculated with Equation 4. Simple myopic astigmatism means that the spherical is emmetropic and the cylindrial is myopic. Compound myopic astigmatism means that both cylindrial and spherical are myopic. Simple and compound hyperopic are determined similarly. Mixed astigmatism means that the cylindrial and spherical are either myopic and hyperopic or hyperopic and myopic [35].

Presbyopia

Presbyopia begins to affect visual ability approximately around the age of 40 [45, p. 81]. This means that the ability to see objects located nearby is weakened.

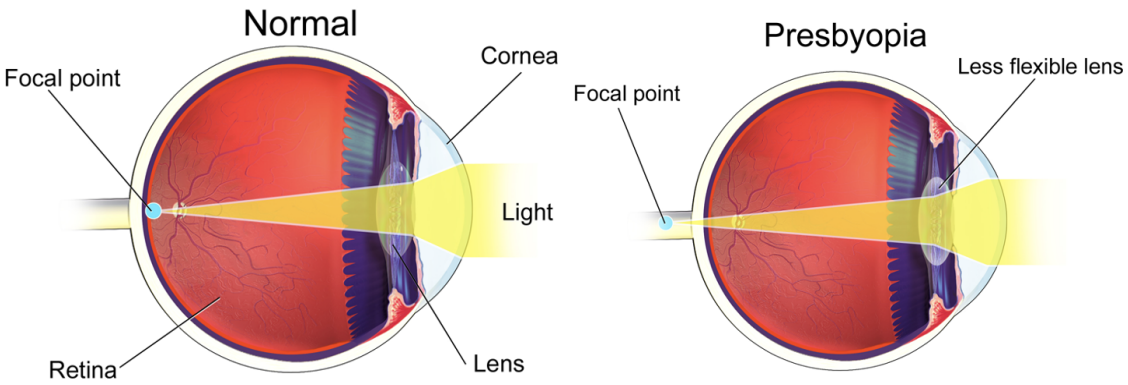

Figure 7: The left side shows how the normal eye works. The lens can adjust the ciliary muscles suitably, so the image is focused in the retina. In the right side, the lens ability to adjust the size of lens is weakened and this can cause situation where the light is not focused into retina. This phenomena can be seen in older people for example when they are reading something and move it further away to be able to focus.

Presbyopia is related to the lens because the flexibility of the lens decreases with age and this makes it more difficult for the lens to accommodate at short distances [45, p. 82]. Along with difficulty seeing close objects, presbyopia can cause symptoms such as headaches, dry eyes, and trouble focusing in dim light. This means that presbyopia can reduce quality of life if it is not corrected with glasses, contact lenses or surgery [46]. The basic principle of presbyopia is shown in Figure 7.

The onset of presbyopia varies across the world. The temperature of the environment has an impact on this, because presbyopia seems to start earlier if the average annual temperature is higher. For example, the mean onset of presbyopia in Finland is 44.5 years, while it is less than 40 years in India [47]. However, the real factor in the background is solar radiation. Radiation near ultraviolet (310nm-400nm) accelerates lens aging [47].

3 Aberrations of the eye

The human eye is a complicated system that focuses light onto the retina, as discussed in Chapter 2. However, some components, for example the cornea and lens, may have distortions, and this can lead to optical aberrations. Distortions have a significant impact because they weaken the vision of humans.

One of the ways to detect distortions can be done with the help of the wavefronts. The wavefront is a line where the points of the wave are in the same phase. Thus, if the wavefront is flat, the wavefront is ideal and the phase of every point is similar. Conversely, if the wavefront is a curve, there are some differences in the phase.

Aberrations of the eye can be categorized into lower-order aberrations (LOAs) and higher-order aberrations (HOAs). The division is based on the possibility of fixing these aberrations. LOAs can be fixed with eyeglasses or contact lenses, and this is not similarly possible for higher-order aberrations. However, it is also possible to fix HOAs with corneal rigid gas-permeable lenses [48]. HOAs can also be fixed, for example, with the help of cataract surgery [49].

In addition to the division of LOAs and HOAs, aberrations can also be divided into monochromatic and chromatic aberrations. Chromatic aberrations are dependent on wavelengths, unlike monochromatic aberrations. The common rule related to refractive index and wavelength is the following: When the wavelength increases, the refractive indices decrease. Monochromatic aberrations are also divided into longitudinal and transverse components. The longitudinal component measures aberration along the optical axis and the transverse component perpendicularly to the optical axis [12, p 251-252].

The example of the aberrated wavefront is shown in Figure 8. The light rays are not focused into the same spot and aberration is created. Aberrations are considered positive if the wave is ahead of the ideal wavefront and negative if the aberrations are behind [1]. The incoming wavefront has aberrations in the pupil plane, and some

parts of it are ahead of the ideal wavefront and others are behind. If the wavefront is ahead, it means that the wavefront is refracted more than it should be. Conversely, if the wavefront is behind compared to the ideal wavefront, the wavefront is refracted less.

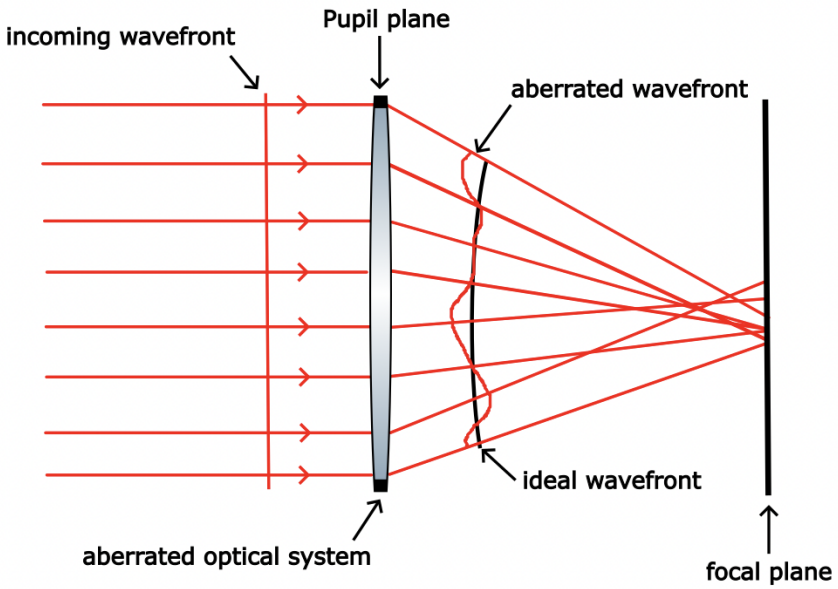

Figure 8: This is a simple example of aberration. The wavefront travels to the optical system and is aberrated. After that, the black line describes the ideal wavefront without any aberrations and the red line describes the aberrated wavefront. Because of the aberrated wavefront, the light beams are not focused into same location in a focal plane.

There are several different factors which affect the aberrations. Pupil size is one of them and usually larger pupil affect more. Age is the second significant factor, and older people have more aberrations than younger people. These changes are related to the cornea and the crystalline lens. Other contributing factors are accommodation and ocular pathologies such as cataracts [50, p 75]. Most human beings have some aberrations, and due to evolution, brains are able to compensate for these aberrations [51].

3.1 Mathematical models in wavefront analysis

Zernike polynomials

Wavefronts can be analyzed with the help of many mathematical models. The most common model is Zernike polynomials. The other options are, for example, Chebyshev's and Bessel's polynomials [52]. The reason for the popularity of Zernike polynomials is based on orthogonality and symmetry properties [53]. Zernike polynomials are monochromatic aberrations, so they are independent of wavelength [12, p 254].

In this chapter, the focus is on the Zernike polynomials. As mentioned earlier, aberrations can be represented mathematically with the help of Zernike polynomials. In addition, Appendix includes Equations 43, 44, 45 and Table V of parameters related to Zernike polynomials [54]. Ordinal number of Zernike polynomials (j) can be easily calculated with Equation 5

$$j = \frac{n(n+2)+m}{2}, \tag{5}$$

where n is the radial index and m is the azimuthal index of Zernike polynomials [12, p 255]. In addition, the radial index can be derived with the help of Equation 6

$$n = \lceil \frac{-3+\sqrt{9+8j}}{2} \rceil, \tag{6}$$

where $\lceil\ \rceil$ is the ceiling operator which rounds up to the next integer. Equation 7 also shows how the azimuthal index is calculated with values j and n

$$m = 2j - n(n+2). \tag{7}$$

Zernike polynomials are shown in Figure 9 which shows the four lowest degree aberrations. Next to every aberration, there is a Z-letter with superscript and subscript describing the degree of radial polynomials and azimuthal frequency. In addition to this, Table I shows the Zernikes polynomials for the first four degree

aberrations. There are many different ways to classify Zernike polynomials and these polynomials are based on OSA/ANSI indices [54].

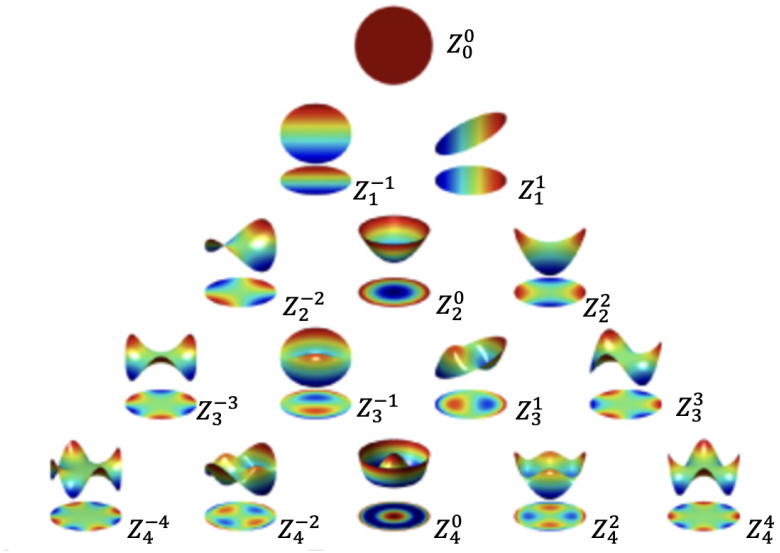

Figure 9: Different Zernike polynomials are shown in this image. The image is adapted from [54]. The superscript correspond to multiplier for azimuthal angle of the Zernike polynomial, while the subscript represents its radial order or degree [55].

Table I: This table shows Zernike polynomial for first four degree aberrations, as a polar representation. The parameter n describes the radial order of the polynomial, m describes the azimuthal angle of the polynomial and the j is ordinal number of polynomial. These Zernike polynomials are under the OSA/ANSI indices [54].

Z_m^n	Z_j (p,θ)	Aberration
Z_0^0	1	piston
Z_1^1	$2\rho\ \cos\theta$	Tilt X
Z_{-1}^1	$2\rho\ \sin\theta$	Tilt Y
Z_2^{-2}	$\sqrt{6}\rho^2\ \sin\ 2\theta$	45° Primary astigmatism
Z_2^0	$\sqrt{3}(2\rho^2-1)$	Defocus
Z_2^2	$\sqrt{6}\rho^2\ \cos\ 2\theta$	0° Primary astigmatism
Z_3^{-3}	$\sqrt{8}\rho^3\ \sin\ 3\theta$	Trefoil
Z_3^{-1}	$\sqrt{8}(3\rho^3-2\rho)\ \sin\ \theta$	Primary y-coma
Z_3^1	$\sqrt{8}(3\rho^3-2\rho)\ \cos\ \theta$	Primary x-coma
Z_3^3	$\sqrt{8}\rho^3\ \cos\ 3\theta$	Trefoil
Z_4^{-4}	$\sqrt{10}\rho^4\ \sin\ 4\theta$	Quadrafoil
Z_4^{-2}	$\sqrt{10}(4\rho^4-3\rho^2)\ \sin\ 2\theta$	45° Secondary astigmatism
Z_4^0	$\sqrt{5}(6\rho^4-6\rho^2+1)$	Primary spherical aberration
Z_4^2	$\sqrt{10}(4\rho^4-3\rho^2)\ \cos\ 2\theta$	0° Secondary astigmatism
Z_4^4	$\sqrt{10}\rho^4\ \cos\ 4\theta$	Quadrafoil

Refractive errors myopia and hyperopia, which were discussed in an earlier chapter, belong to defocus aberration. Astigmatism can have primary and secondary forms. Defocus and primary astigmatism are second-order aberrations when secondary astigmatism is fourth-order aberrations. It is also important to notice that aberrations near the center vertical line of the Zernike pyramid have a greater impact on visual acuity than aberrations away from the center [12, p 284]. Thus, defocus

and spherical aberration should have a greater impact on visual acuity when astigmatism affects less.

3.2 Lower-order aberrations

0, 1st and 2nd order aberrations belong to lower-order aberrations and 85 % of all aberrations are low-order aberrations [40]. The typical low-order aberrations are defocus and astigmatism [20, 40].

0 and 1st order aberrations

Piston is a zero-order aberration. It describes the shift from the ideal wavefront. It is not normally measured [56, p 27]. Zernike polynomial for the piston is Z_0^0. First-order aberrations are tip and tilt. The tip aberration describes the angular rotation around the horizontal axis, and the tilt aberration describes the rotation around the vertical axis, as shown in Figure 10. It is important to notice that the background outside the circle is equal to the non-aberrated signal. This means that a bluish color refers to a weaker signal and a yellowish color refers to a stronger signal. Zernike polynomials for tip and tilt are Z_{-1}^1 and Z_1^1. Zero- and first-order aberrations do not affect the quality of the image [57].

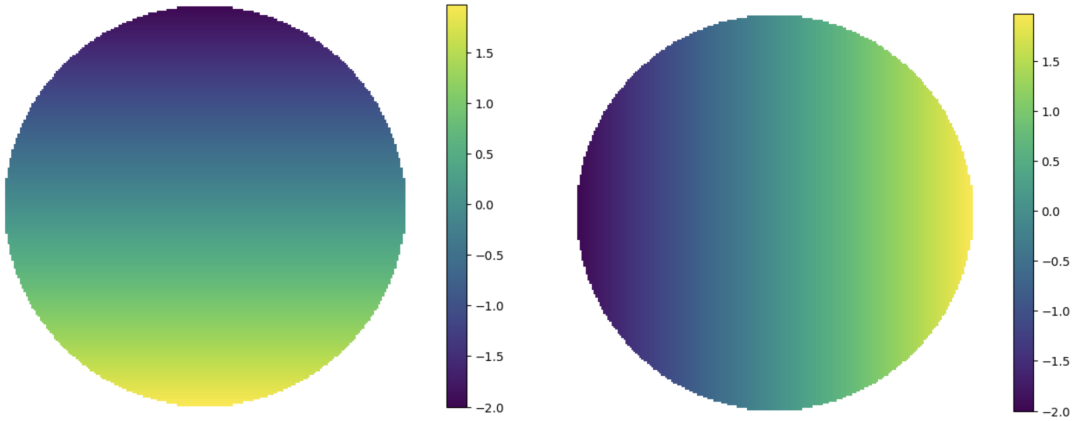

(a) (b)

Figure 10: a) This shows the wavefront map of the tip. The signal is normal in the center. However, there is deviation in the signal in vertical direction. b) This is almost similar than tip wavefront map. The signal deviation happens now in horizontal axis. Both of these images are simulated with Python.

2nd order aberrations

Defocus is one of the most common aberration types. It refers to myopia and hyperopia. Defocus can be positive (myopia) or negative (hyperopia) [1]. The defocus increases when the size of the pupil increases [50, p 72]. There is only one aberration for defocus in Zernike polynomials and it is Z_2^0.

Astigmatism is a second common second-order aberration. In addition to that, astigmatism also has fourth-order polynomials. Thus, astigmatism has several Zernike polynomials and those are Z_2^{-2}, Z_2^2, Z_4^{-2} Z_4^2. These second-order aberrations are primary aberrations and fourth-order aberrations are called secondary astigmatism. Figure 11 shows an example of aberration maps of defocus and astigmatism.

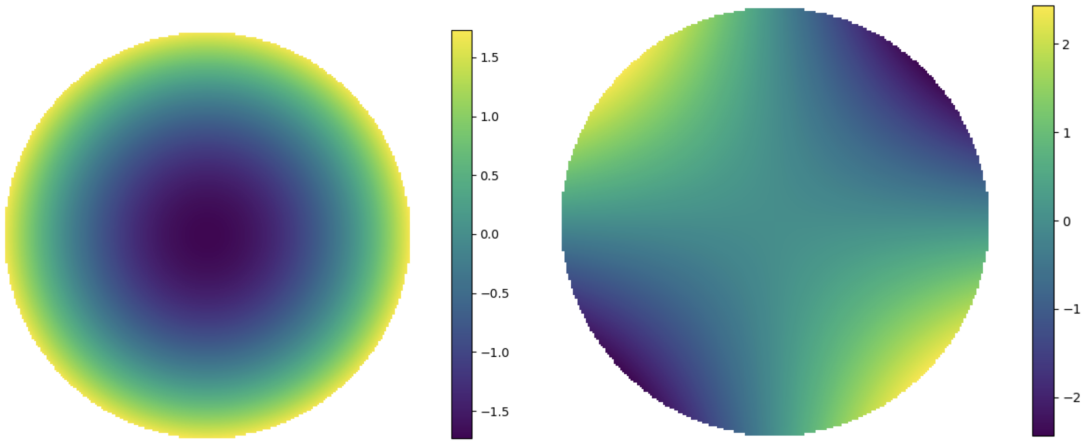

(a) (b)

Figure 11: a) The wavefront map of defocus (Z_2^0) can look like this. The middle point has a weaker signal and the signal becomes stronger when moving farther from the center. b) The wavefront map of oblique astigmatism (Z_2^{-2}) looks like this. The point is strecthed in 45 angle compared to the horizontal axis. Both of the wavefront maps are simulated with Python and they have own color scales to show the contrast.

3.3 Higher-order aberrations

HOAs include about 15 % of all aberrations and are more complex than lower-order aberrations, so their correction is more difficult. HOAs include third-order aberrations and those of even higher order [40]. In this section, trefoil, quadrafoil, coma and spherical aberration are determined.

Trefoil and Quadrafoil

Trefoil is a third-order aberration. Trefoil aberration gets its name from its characteristic three-fold symmetry, which resembles a triangular distortion pattern in the wavefront error. Trefoil is a third-order aberration with the Zernike polynomials Z_3^{-3} and Z_3^3. In trefoil aberration, the peripheral vision is usually more affected [50,

p 73].

Similarly, quadrafoil is named for its four symmetrical lobes, which form a distinctive pattern in the wavefront error. Quadrafoil is fourth-order aberration and its zernike polynomials are Z_4^{-4} and Z_4^4. Aberration maps for the trefoil and quadrafoil are shown in Figure 12.

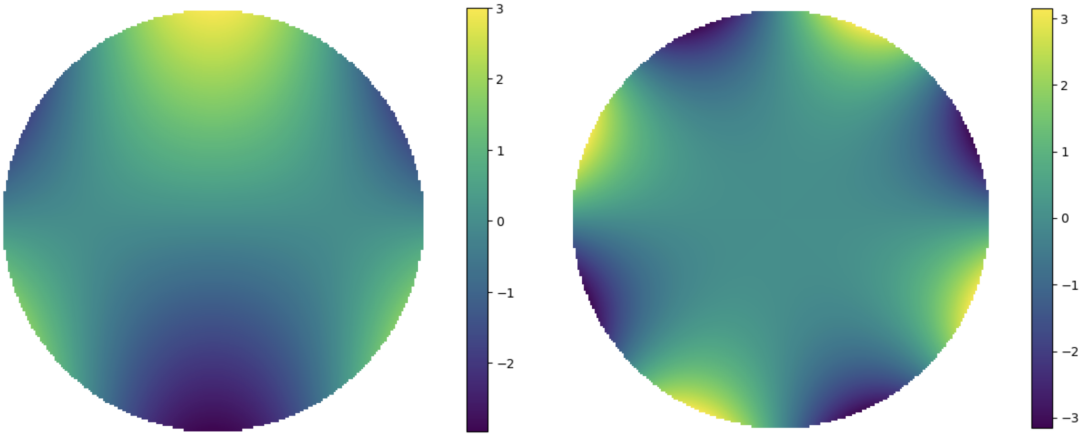

a b

Figure 12: a) Trefoil aberration has threefold symmetry and thus three stronger signal areas are distinguishable in the peripherals. This example is Z_3^{-3}. b) Similarly than trefoil, quadrafoil forms four distinguishable signals in the peripherals. Zernike polynomial for this is Z_4^{-4}. Both of the images are simulated with Python.

Coma

Coma refers to a distortion in image formation where light rays are not focused at the same point in the image plane. The formed point is stretched and looks comet-like [40]. The Zernike polynomials for coma are Z_3^{-1} (vertical coma) and Z_3^1 (horizontal coma) and the example of the aberration map for coma is shown in Figure 13.

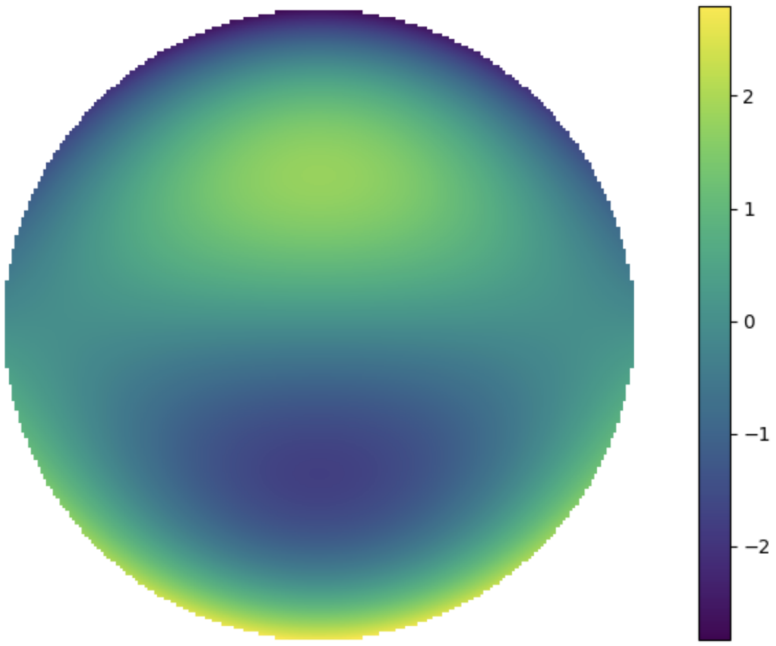

Figure 13: Coma aberration can be either vertical or horizontal. This image shows example of vertical coma Z_3^{-1}. This is simulated with the help of Python.

Spherical aberration

When light rays pass near the edges of lenses or mirrors, there may be blurring in the image. The rays near the edges are not focused in the focal point like other rays [40]. The spherical aberration can be longitudinal (LSA) or transverse (TSA). Longitudinal means that the image is not formed in the paraxial image plane and transverse means that the rays are not targeted into the same spot in the paraxial image plane. LSA is measured along the optical axis and TSA perpendicularly to the optical axis [58, p 116].

Spherical aberration can also be divided into positive or negative. In positive spherical aberrations, the peripheral rays are refracted more than the central rays. In contrast, negative spherical aberration occurs when the peripheral rays are refracted less than the central rays [57]. The aberration map of spherical aberration recalls the defocus aberration and its Zernike polynomial is Z_4^0. However, the largest deviation

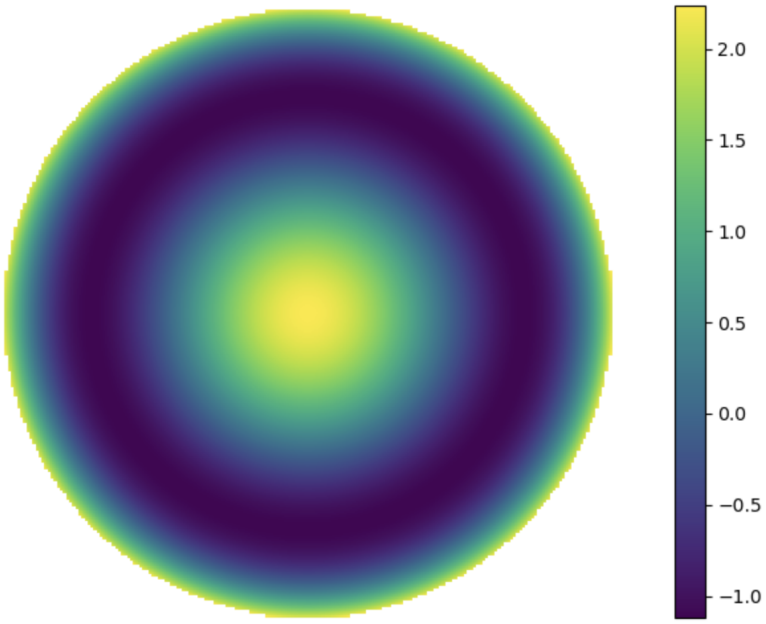

Figure 14: Spherical aberration reminds defocus, but the strongest signal is coming from the centre, instead of the peripherals. This is simulated with the help of Python.

is in the middle of the aberration map with spherical aberration, as shown in Figure 14, while it is in the edges with defocus.

3.4 Clinical measurements of aberrations

One of the common ways to find out possible distortions in vision can be done with Snellen chart, which is surely familiar to most of us. The Snellen chart includes several rows of letters. The first row has the largest letters, and they become smaller after every row. At the same time, the number of letters increases. The test is completed by standing six meters away from the chart and one eye is covered and the other eye is used to try to see the letters. This is done for both eyes. Visual acuity is normal if vision is 20/20. The latter number tells the distance to which the letter can be seen with normal visual acuity. For example, 20/100 means that a person with normal vision can see the same letter at a distance of 100 feet [59].

The cornea plays a significant role in vision and is responsible for 2/3 of refractive power, as discussed in Chapter 2. Scheimpflug camera is one way to measure corneal aberrations. It is based on the principle that the sensor plane and the lens plane are not parallel and both of them, together with the image plane, form an intersection of their lines [60]. Another way is to use corneal topography which gives a three-dimensional map of the cornea's flat and steep areas. There are also corneal topography that is based on the LED technology. Other possible techniques are retinoscopy, autorefraction and aberrometry. All of these techniques are objective, but there are also some subjective ways to measure aberrations, such as trial frames and phoropter. Objective methods are also important because they take into account neural processing [61].

4 Wavefront sensing

As discussed in a previous chapter, aberrations can be measured in several ways. This chapter focuses on how aberrations are measured with wavefront sensing technology. In addition to measurement, it is possible to fix these aberrations with the help of adaptive optics (AO). Wavefront sensing and adaptive optics are also widely used in astronomy.

4.1 Shack-Hartman wavefront sensor

Shack-Hartman wavefront sensor (SHWFS) is a simple way to measure aberrations of the eye, improve images of the cosmos and check the laser beam quality. SHWFS is also often used in AO. In addition to the SHWFS, this chapter handles other types of wavefront sensor, AO and some applications of WFS.

History

The SHWFS is based on the Hartman screen test. This test was created by Johannes Hartman (1865-1936), who was a German astrophysicist. The reason for this test was the poor quality of telescope and Hartmann wanted to find out the source of the problem [62].

Hartmann built a screen full of holes and placed this over the aperture of the lens. In addition, photographic plates were inserted around the different focal points. These exposed plates represent a spot diagram. By matching the corresponding spots from the two plates and knowing the distance between the exposure locations, the concentration of the rays in the neighborhood of focus can be determined [62].

SHWFS reminds of this Hartmann test and was also built to solve a problem. In this case, the problem was that the images of the satellites were not good enough because the atmosphere of the Earth limits the image quality. Roland Shack was one of the people who worked with this problem, and he realized that the only reasonable solution was to replace the holes in the plate with lenses [63]. This system is called a lens array.

Another significant person who participated in the development of the lens array was Ben Platt. Platt and Shack developed a method for preparing lens arrays. Even though commercial lens arrays were available, they were inappropiate due to their focal lengths. Platt and Shack invented a fabrication system where concave grooves were created in the glass. The grooves were prepared with the help of nylon rod and the width of the grooves was 1 mm. This procedure was repeated and an array of grooves was formed in the glass plate [62].

Structure

SHWFS consists of a microlens array and a detector [2, p 5]. The diameter of the microlenses typically varies between 100-600 μm. Each microlens creates a spot of

the incoming light on the detector. The difference between the ideal location of the spot and the actual location of the spot indicates the aberrations. The size of the lenslet significantly affects the wavefront sensing. Smaller diameter microlenses can create more accurate wavefronts [3].

There are two common types which are used as a sensor in SHWFS. Charge-couple device (CCD) is another of them. CCD is a semiconductor where the charges of the light-sensitive pixels are converted to signals.The charges are converted to circuit which locate outside and this circuit converts them to signal [64]. The advantage of CCD is good quality for images and electrical consumption and possible artifacts are seen as disadvantages [65].

Similarly, complementary metal-oxide-semiconductor (CMOS) is also the semiconductor, but it works differently compared to CCD. In CMOS, Condensators are put parallel to each individual pixel. The pixel collected in the condensator are converted directly into voltage by the electronic circuit of every pixel [64]. The advantage of CMOS is the rapidity. On the other hand, increased noise and smaller fill factor are disadvantages.

The principle of the SH sensor is shown in Figure 15. The left side describes the flat wavefront and the right side describes the aberrated wavefront. Microlenses focus the light onto the camera sensor, where the light spots are seen as white dots. It can be clearly seen that the aberrated wavefront makes the distances of spots unconstant while the flat wavefront makes the distances constant. This can also be noticed from the camera sensor because the aberrated wavefront makes the pattern of the spots look strecthed and tilted [4].

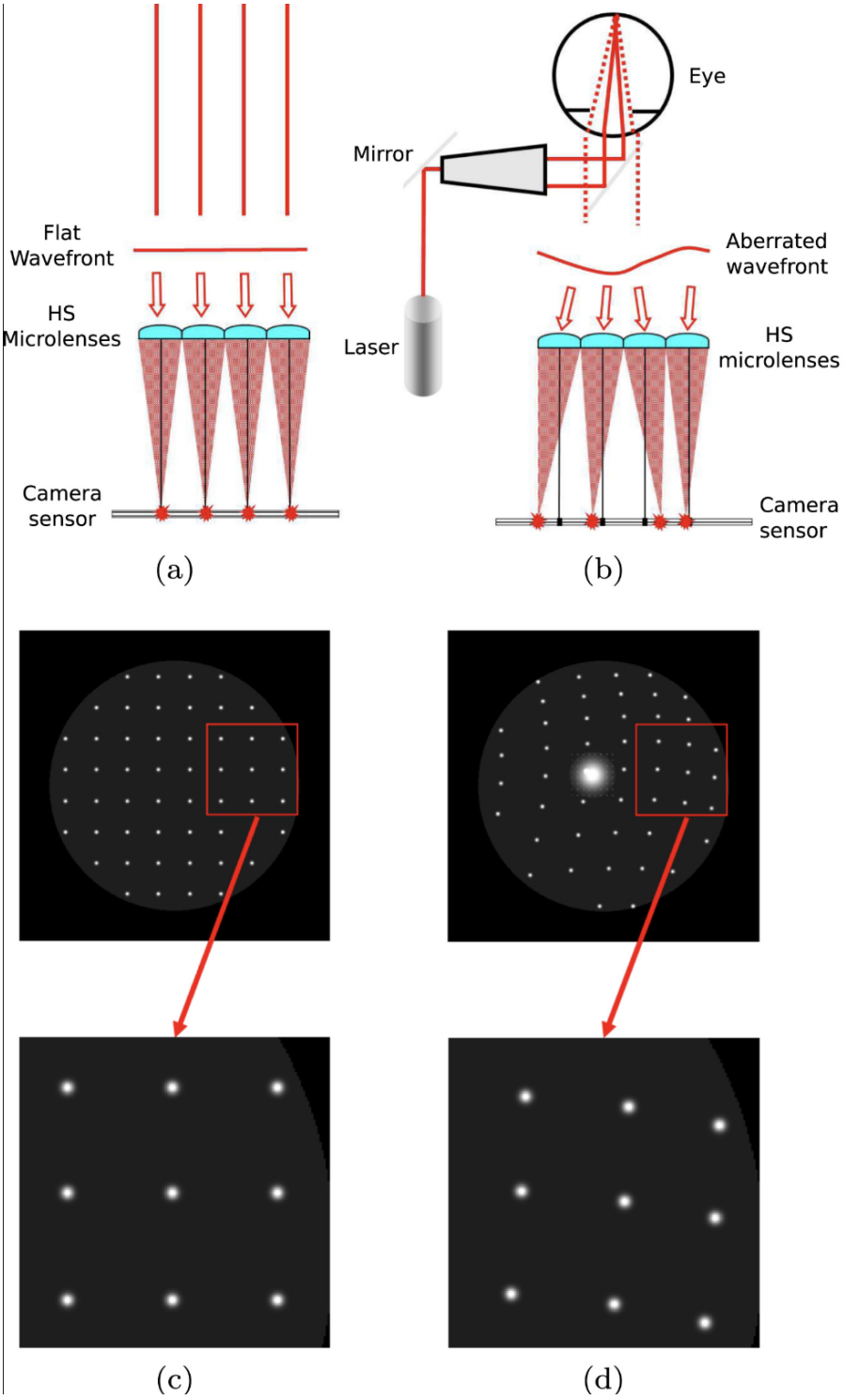

Figure 15: The non-aberrated wavefront is shown in the left side (a) and aberrated wavefront in the right side (b). When the wavefront is flat, the points in camera sensor are arranged at the same distance from each other (c). If the wavefront is aberrated the light is not directly transmitting the microlenses and this cause the focus of the point to locate with unconstant distances (d). In the camera sensor, the light points are aligned with the flat wavefront. In the case of aberrated wavefront, the light points are tilted and the structure looks strecthced [4].

4.2 Other types of wavefront sensors

Pyramid sensor

A pyramid sensor is the second type of wavefront sensor. It is a four-faceted prism that naturally forms four different images in the focal plane. The intensity distributions in the facets differ in the case of wavefront aberrations [5]. The advantage of the pyramid sensor is the ability to measure low- and high-order aberrations more accurately than SHWFS [66]. On the other hand, the pyramid sensor includes high-precision optics and modulation, which increases the costs. The pyramid sensor has already replaced SH-WFS in astronomy [5]. The example of the pyramid sensor is shown in Figure 16.

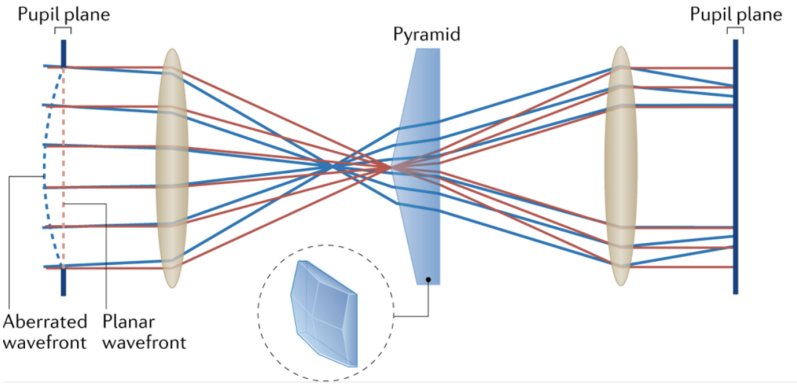

Figure 16: The main part of the pyramid sensor is a four-faceted prism and it forms four different images. The first mirror before pyramid sensor is a concave mirror and it focuses light into the pyramid. The later mirror is also the concave mirror and it collimates the light into the pupil plane [67].

Shearing interferometer

A shearing interferometer is third common type of wavefront sensors. The wavefront of this system is not compared to any other reference wavefront. Instead, it is based on the interference between two sheared wavefronts, as shown in Figure 17. Shearing interferometer can also be divided into three types. Those are lateral, azimuthal,

and radial types. Lateral shearing interferometer bases on the location difference in lateral direction, whereas azimuthal shearing interferometer focuses on the difference between the azimuthal angles. Radial shearing interferometry differs from these two methods because it focuses on the difference between contracted and extended wavefronts [6]. Figure 18 shows examples of these three types.

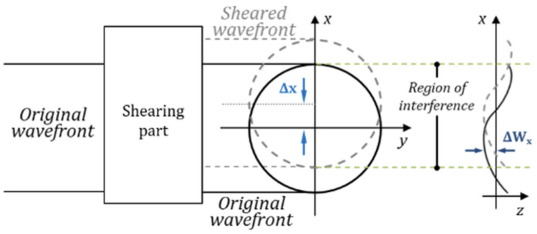

Figure 17: This is example of the layout of the shearing interferometer. It divides the the wavefront into two different parts and those are sheared wavefront and original wavefront. In this method, the wavefront is not compared to any kind of form. This method is based on interference fringes [6].

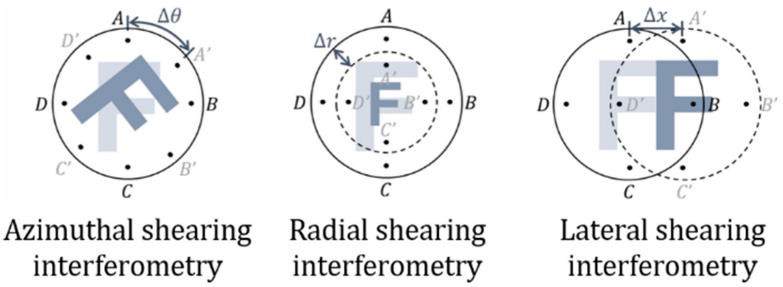

Figure 18: Three types of shearing interferometers are shown in this image. In azimuthal shearing the azimuthal angles are different with sheared wavefront while radial shearing creates contracted and extended wavefront. Lateral shearing interferometry creates two wavefronts which differ from the lateral location [6].

4.3 Wavefront sensors in adaptive optics

Adaptive optics (AO) is closely linked to wavefront sensors. This chapter tells about the connection between adaptive optics and wavefront sensor, wavefront correctors and, in addition, how adaptive optics is used in astronomy.

History and connection to wavefront sensing

The first concepts related to AO were studied in the 1950s. For example, in 1953, Horace Badcock proposed the idea of building AO system. Another example is from 1957, when Vladimir Linnik introduced the same idea, so AO is not a particularly old invention. Practical applications were developed in the 1960s, with the first target to image satellites and project laser beams into space. The first AO images of cones were taken only in 1997 [68].

AO consists of three different parts: wavefront sensor, control computer and wavefront computer, as shown in Figure 19. The aberrated wavefront the eye is directed towards the Shack-Hartman wavefront sensor (SHWS) and the measured data is converted into AO control computer. AO control computer handles the data and sends signal to the deformable mirror (DM). This signal includes information about how the form of the mirror must be changed. This makes the wavefront ideal, and the light can be directed to imaging detectors and better images are achieved [7].

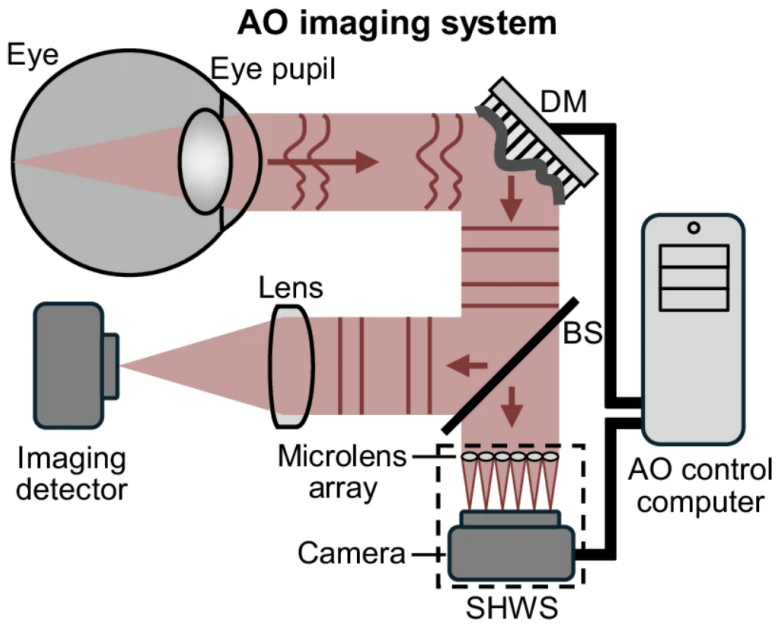

Figure 19: Model of adaptive optics is shown in this image. First, the aberrated wavefront from the eye reflects from the deformable mirror towards the beamsplitter (BS). In the BS, part of the light reflects towards to the imaging detector and the rest of it into the SHWS. In the SHWS, the data of aberrated wavefront is sent to the AO control computer. Control computer analyzes the data and make needed changes in the DM. DM fixes the aberrations of the wavefront which makes the aberrated wavefront to become ideal [69].

Wavefront correctors

There are many options when choosing an appropriate wavefront corrector. The DM with the actuators is one of them. It is based on a continuous reflective mirror and actuators which can create deformations in the surface. The second significant wavefront type is piston-only segmented corrector. It consist of array of planar mirrors. Piston-only can only change piston mode, but it is also possible to have segmented corrector that can correct piston, tip and tilt [3]. These three types of wavefront correctors are shown in Figure 20. On the other hand, deformable mirrors have gaps between the mirrors and this weakens the quality of corrections.

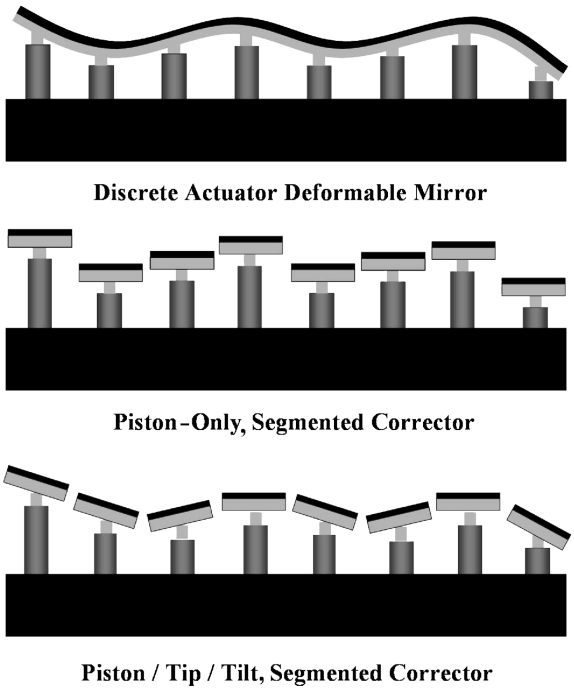

Figure 20: This image shows three different types of wavefront correctors. Discrete actuactor has continous reflective surface and it is controlled with the help of actuators which locate below the surface. Piston-only and piston/tip/tilt segmented correctors are similar except for the degrees of freedom [70].

Other examples of wavefront correctors are membrane mirrors and bimorph mirrors. A membrane mirror consists of a flexible and reflective membrane, a top electrode and an array of electrodes that locate below the reflective membrane. Without voltage, the reflective membrane is flat. When voltage is applied, it incudes electrostatic forces which change the shape of the reflective membrane. Bimorph mirrors consist of piezoelectric material that is sandwiched between electrodes below and top electrode, similarly to a membrane mirror. When the voltage is supplied, the piezoelectric material changes shape. The magnitude of the deformation depends on the material and the strength of electrical field [3].

Adaptive optics in astronomy

AO is often used in astronomy. The first proposal of using adaptive optics in astronomy was made as early as 1953, but it took 20 years when the first demonstration of that was made. The most common wavefront sensor is Shack-Hartman, and the most common wavefront corrector is a deformable mirror [71].

Atmospheric turbulence is the reason for the blurry images because it creates aberrations to the wavefronts. This causes the point-spread function to spread out and causes worse resolution. AO makes it possible to study many areas, like exoplanets, stellar populations, and even the black hole in our galaxy [71]. Anisoplanatism is an important phenomenon related to astronomical imaging. This means that the wavefront distortions depend on the angle of view. Thus, AO does not work similarly in the whole field of view. This makes it difficult to study large areas at the same time [72].

Adaptive optics in ophthalmology

AO is often combined with another imaging technology. The three most common techniques are flood illumination (FLO), scanning laser ophthalmoscopy (SLO) and optical coherence tomography (OCT). FLO was the first AO system to utilize closed-loop technology. With FLO, it is possible to image cones and retinal vessels [73]. In addition to cones and retinal vessels, SLO can take images of rods and retinal ganglion cells [73] and even detect glaucoma [74]. OCT is the most developed technique of all due to capability to take cross-section images with best resolution [75]. OCT can be used to diagnose, for example, choroidal neovascularization or macular edema [76].

5 Experimental system design

The design of the aberrometry system is shown in Figure 21. This is drawn with Inkscape (v 1.3.2) and includes all the main components along the path of light. In addition, a sensor protection and a trial lens holder are modeled with Fusion360 (v 2602.1.14, Autodesk, USA), as will be shown in Chapter 6.

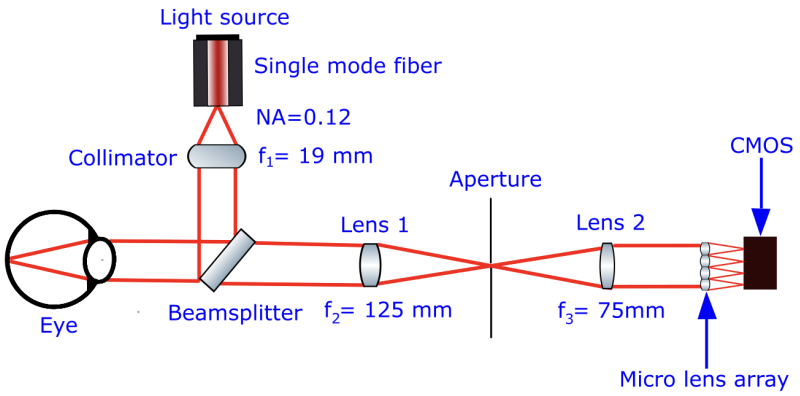

Figure 21: The light from the light source is directed to the retina and after that it is reflected backwards and the retina is finally imaged in the CMOS sensor. The red lines describe the path of the light. This image is drawn with Inkscape.

5.1 Illumination and optic relay

As seen in Figure 21, the laser diode (light source) is the first point of this aberrometer. The light from the laser diode is collimated with the help of an achromatic doublet (f=19 mm). This makes it possible to create a laser beam with appropriate size for the eye, about 4.5 mm. After that, the light hits the beamsplitter and part of the light penetrates it and continues traveling away from this system. The beamsplitter type is (10:90 R:T) which means that 10 % of the light is reflected to the eye and 90 % of the light is transmitted through the beamsplitter, away from the aberrometer. When the light arrives at the cornea, the focus is started and the light is finally focused on the retina where it reflects backward.

The reflected light hits again the beamsplitter and now the passed light is the most interesting part. Due to the optical thickness of the beamsplitter, the passed light is in the off-axis phase. This problem is solved with translating the cage segment plate laterally, which transfers the light back to the center of the cage system. The passed light encounters the telescope system and the pinhole between it. The purpose of the pinhole is to minimize the reflections of the cornea. Lens 1 focuses the light into the pinhole and only collimated light rays are capable of passing through the aperture. The pinhole locates inside the XY translating lens mount and both lenses locates inside the cage plate is used in lenses 1 and 2. After lens 2, the light is collimated and the light rays hit the microlens array (MLA) (f=5.4 mm). This array focuses the light into the CMOS, which creates the image of light spots. MLA is located inside the cage rotation. The last part of this system is the CMOS camera. The models and the manufacturer of these components are shown in Appendix (Table VI). In addition, some components are used with the model eye, and this is explained in more detail in Section 6.4.

5.2 Determining the system parameters

Laser diode parameters

There are several physical principles that are taken into account when building this optical system. First, the appropriate laser beam must be chosen. The wavelength can not be in the ultraviolet range or shorter because it could be a risk to health. The wavelength should not also be in the range of visible light because it may annoy the eye and make measurements unpleasant and difficult. The best possible wavelength area is in the near infrared range. The wavelength of the beam is chosen to be 850 nm, because the absorption of water is small. This is important because the eyes consist mostly of water and with longer wavelengths it could be difficult to get enough signal [77]. Figure 22 shows the water absorption curve as a function

of wavelength. In addition, the laser with 635 nm wavelength was also used as a reference laser. Because the wavelength of this laser is in the visible-light range, it makes alignment easier.

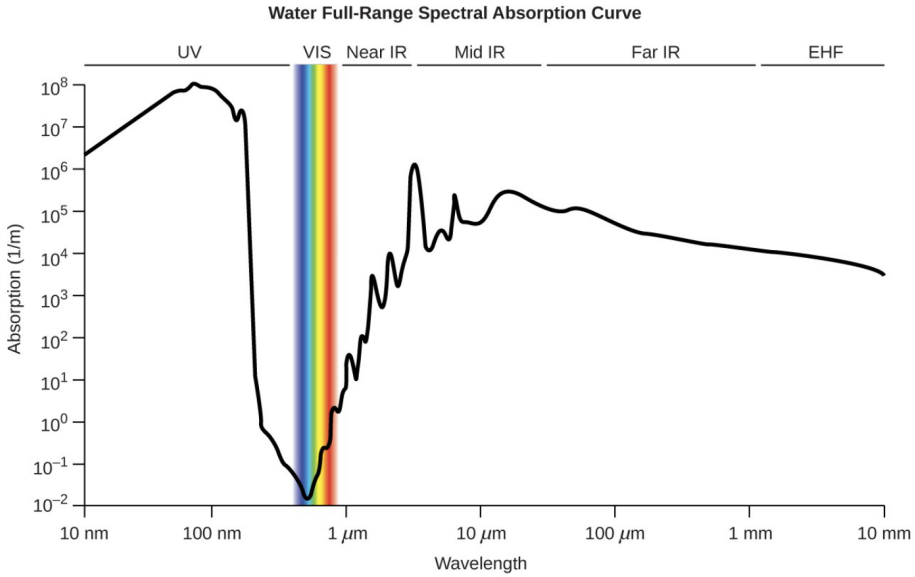

Figure 22: This absorption curve shows how the absorption changes as a function of wavelength. The visible light wavelengths have smallest absorption but it irritate eyes so it can not be used [77].

In relation to the laser beam, another important factor is the size of the laser beam. The size of the pupil is approximately 4-5 mm, so the diameter of laser beam should be smaller. The diameter of the laser beam can be calculated with Equation 8

$$w_f = \frac{\lambda f}{\pi w_o}, \tag{8}$$

where w_f is the radius of the focused beam, λ is the wavelength of the light, and w_o is the radius of the collimated beam. The equation for the diameter of the focused beam as a function of the diameter of the collimated beam can be solved by putting $w_f = \frac{D_f}{2}$ and $w_o = \frac{D_c}{2}$, as shown in Equation 9

$$D_f = \frac{4\lambda f}{\pi D_c} \tag{9}$$

where D_f is the diameter of the focused light and D_c is the diameter of the collimated light, which means that every light ray is directed in the same direction. The wavelength is directly proportional to the diameter of the focused light. The calculated value for the diameter of the focused beam is calculated in Equation 10

$$D_f = \frac{4 \cdot 850 \cdot 10^{-9}\ \text{m} \cdot 17 \cdot 10^{-3}\ \text{m}}{\pi \cdot 4.2 \cdot 10^{-3}\ \text{m}} = 4.38\ \mu\text{m}, \tag{10}$$

where the wavelength value $850 \cdot 10^{-9}$ m is the same as the optical fiber used, $17 \cdot 10^{-3}$ m is the focal length of the eye and $4.2 \cdot 10^{-3}$ m is the size of the pupil [15].

Figure 23 shows how different wavelengths affect the diameter of the focused beam. With shorter wavelengths, it is possible to achieve a smaller spot.

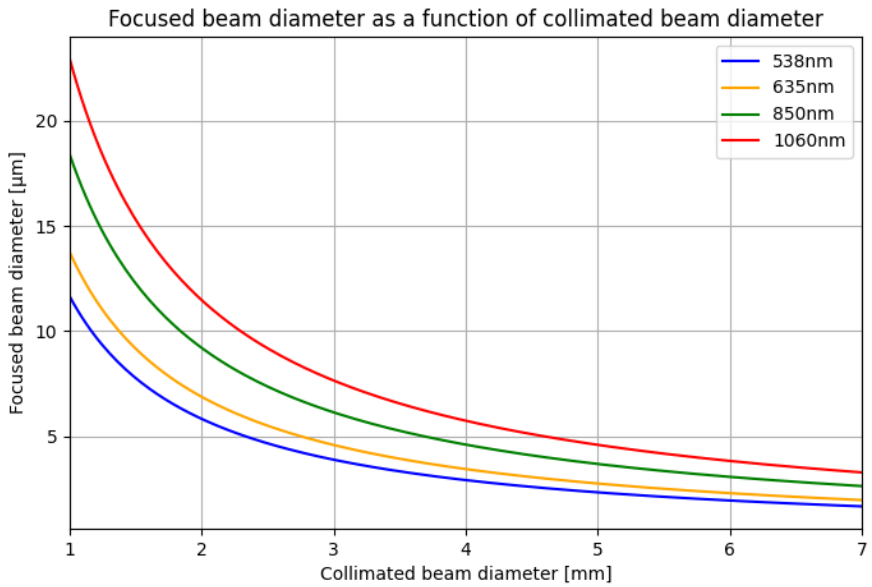

Figure 23: The wavelength has a clear impact on the size of the focused beam diameter. Smaller wavelengths make possible to achieve smaller focused beam diameter compared to similar collimated beam diameter with larger wavelengths. In this aberrometer, 635 nm and 850 nm wavelengths are used.

The waist of the beam describes the minimum radius of the beam. The radius of the beam in the waist area can be calculated with Equation 11

$$\omega(z) = \omega_o \sqrt{1 + \frac{\lambda z}{\pi \omega_o^2}}, \tag{11}$$

where ω_o is the radius of the beam waist, λ is the wavelength and z is the distance from the beam waist. The radius of the beam waist is equal to the radius of the spot. The purpose of calculating the beam waist is related to the pinhole. If the beam waist is known, it is possible to solve how accurate the pinhole must be in the telescope. This makes it possible to reduce the amount of unwanted light reaching the SHWFS. Rayleigh range is an important factor related to the waist of the beam because it describes the distance at which the cross-sectional area of the beam doubles [78]. In this aberrometer system, it tells the interval where the pinhole can be moved. Equation 12 shows how the Rayleigh range can be calculated

$$z_r = \frac{\pi \omega_o^2}{\lambda}, \tag{12}$$

where ω_o and λ describe the same parameters as in Equation 11. The Rayleigh range of the used laser diode can be calculated with the help of parameter NA. Because the refractive index of air is 1 and $sin\theta \approx \theta$ the NA=θ. It is also known that $\omega_o = \frac{\lambda}{\pi\theta}$ so combining these the rayleigh range can be calculated with Equation 13

$$z_r = \frac{\lambda}{\pi NA^2} = \frac{850 \cdot 10^{-9} \text{ m}}{\pi \cdot 0.12^2} = 18.8 \text{ µm} \tag{13}$$

where the value for the Rayleigh range is 18.8 µm. The value of the Rayleigh range increases linearly as a function of wavelength, as shown in Figure 24.

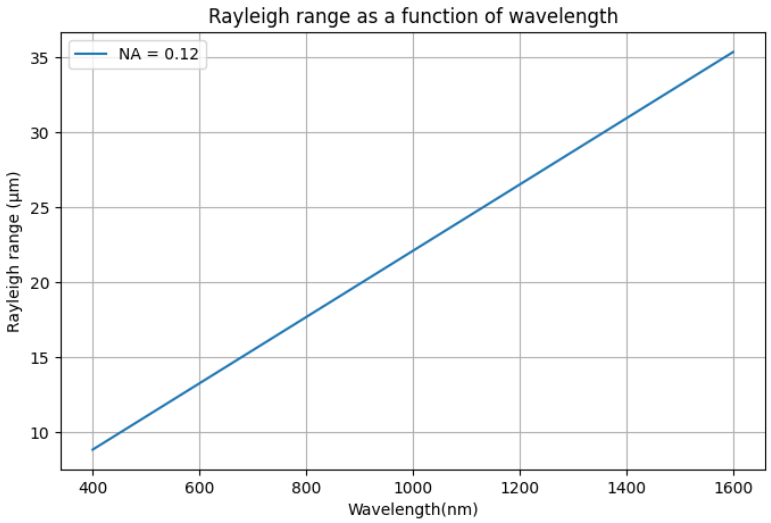

Figure 24: Rayleigh range is calculated with equation $z_r = \frac{\lambda}{\pi NA^2}$ where NA is constant with value 0.12. This NA value is similar to that of laser diode. Rayleigh range increases linearly when wavelength is increased.

It is also important to take into account the optical power of the laser beam. The maximum power allowed for the eye is 750 µW. Before starting the measurements for the eye, this must be measured and possibly attenuated with the help of ND filters. The measurements are done after the beamsplitter. The transmittance of light can be calculated with Equation 14

$$T = 10^{-OD} \tag{14}$$

where T is the transmittance and OD is the optical density.

The point spread function (PSF) describes the response of the imaging system to a point source. It is also a normalized intensity distribution of the point-source image. The real images of the object are formed by the convolution. This means that the object function and the PSF combine to create a new function, which illustrates how the object is imaged [79]. The factors that affect the PSF are aberrations, scattering, diffraction, and defocus [12, 80]. If diffraction is the only factor present,

then the PSF is called a diffraction-limited PSF. This represents the best possible PSF image and this diffraction pattern is called airy disk. The angular radius of the airy disc is shown in Equation 15

$$\Theta = \frac{1.22 \cdot \lambda}{D}, \tag{15}$$

where λ is the wavelength of the light and D is the diameter of the PSF.

CMOS and MLA parameters

The image of the spots is captured with a CMOS camera. Quantum efficiency (QE) describes how efficiently the camera can convert photons to an electric signal. With this camera, the QE depends on the wavelength. With a wavelength of 850nm, the QE is 40%, as seen in Figure 25.

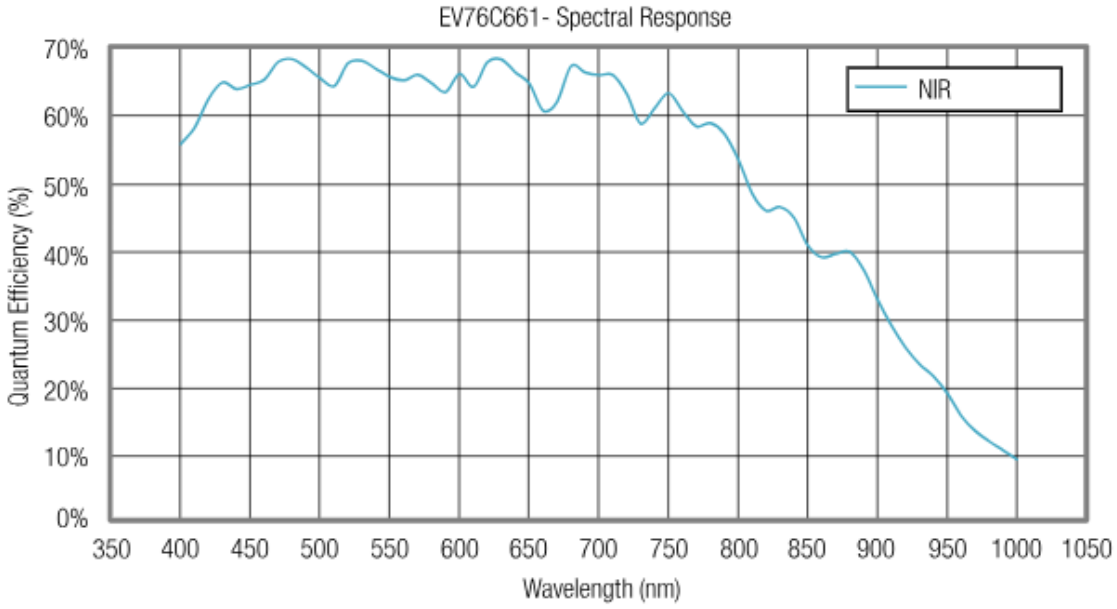

Figure 25: Quantum efficiency depends on the wavelength. The best QE values are obtained when the wavelength is between 450-750 nm. With larger wavelengths, QE weakens significantly. Wavelength of the laser diode is 850nm and the, obtaining QE value about 40%. This graph is copied from the website of Ximea [81].

As discussed in Chapter 4, the microlenses and the CMOS camera form SHWFS in the optical system. The purpose of the microlens array is to focus light rays on the CMOS sensor. The size of the CMOS pixel is 5.3 μm. Because pixels are squares, the area of one pixel can be calculated with Equation 16

$$A_p = (5.30\ \mu\text{m})^2 = 28.09\ \mu\text{m}^2, \tag{16}$$

where A_p is the area of the pixel. It is also known that the sensor has 1.3 million pixels, so the area of the whole sensor can also be calculated with Equation 17

$$A_s = A_p \cdot N_p = 28.09\ \mu\text{m}^2 \cdot 1310720 = 36818124.8\ \mu\text{m}^2 = 36.8\ \text{mm}^2, \tag{17}$$

where A_s is the area of the sensor and N_p is the number of pixels.

The fill factor determines the ratio between the area of the imaged pupil and the total area of the CMOS sensor. The value varies between 0 % and 100%. If the value is 100%, then the whole sensor area is utilized to collect light [2]. In this study, the target fill factor is about 80%. This leaves some space in case of larger pupil size than is excepted. We know that the aspect ratio of the sensor is 5/4, so height is a limiting factor for pupil size. The height can be solved with the quadratic Equation 18

$$5 \cdot x \cdot 4 \cdot x = 20x^2 = 36.8\ \text{mm}^2 \tag{18}$$

where x is the size factor. Because the height is equal to 4x and the value for x is 1.356 mm, the height is 5.426 mm. The average pupil size for humans is 4.2 mm [15]. The fill factor in the sensor is the pupil size divided by the sensor height, as shown in Equation 19

$$FF = \frac{4.2 \text{ mm}}{5.426 \text{ mm}} = 0.774 \approx 77 \text{ \%}, \tag{19}$$

where FF is the abbreviation for the fill factor. FF is quite close to the target value and therefore acceptable.

Spot sampling

In addition to parameters of laser diode, CMOS, and microlenses, other components are also playing an important role, especially in spot sampling. Before the light reaches the sensor, the telescope system must be taken into account. It is important to notice that the eye and lens 1 form the first telescope and lens 2 and microlens array form the second telescope. Lenses 1 and 2 have the same focal lengths, so they do not affect the size of the spots. Equation 20 shows the equation for the magnification

$$M = \frac{f_{mla}}{f_{eye}}, \tag{20}$$

where f_{eye} is the focal length of the eye and f_{mla} is the focal length of the microlens array. As seen, magnification can be calculated as a ratio of focal lengths of microlens array and eye. The focal length of the eye is 16.67 mm and 5.6 mm with micro-lens array so the magnification is 0.329. The value of the diameter of the focus beam D_f is already calculated in Equation 10. With the help of this value, the size of the spot in the lenslet can be calculated with Equation 21

$$D_{spot} = M \cdot D_f = 0.329 \cdot 4.38 \text{ µm} = 1.44 \text{ µm} \tag{21}$$

Because the diameter of the imaged pupil and the diameter of a single lenslet are known, it is easy to calculate how many lenslets are used to sample the pupil image,

as shown in Equation 22

$$N_{lenslets} = \frac{d_{pupil}}{d_{lenslets}} = \frac{4.2 \text{ mm}}{150 \text{ µm}} = 28, \tag{22}$$

where $N_{lenslet}$ is an important factor because the number of Zernike coefficients depends linearly on the number of lenslets. It is known that these two values are almost the same. It can be supposed that with 28 lenslets it is possible to get 28 coefficients reliably because each lenslet determines the area where a single spot can move, as shown in Equation 23

$$J = \frac{(N+1)(N+2)}{2} - 3, \tag{23}$$

where N is the order of Zernike modes and J is the amount of lenslets. Acquiring too many coefficients may cause unexpected problems in reconstructed wavefront aberrations. This means that aberrations can be calculated up to the sixth order [3].

Although the lenslet diameter is 150 µm, the spot can not be as large. The reason for this is diffraction, and the wavelength and focal length of the micro lens array affect it, as seen in Equation 24

$$d_{lenslet} = \frac{4 \cdot 850 \cdot 10^{-9} \text{ m} \cdot 5.6 \cdot 10^{-3} \text{ m}}{\pi \cdot 150 \cdot 10^{-6} \text{ m}} = 40.4 \text{ µm}, \tag{24}$$

where familiar values for wavelength, focal length, and lenslet pitch are used. Equation 25 shows how the pixel sampling value PS can be calculated by dividing this value by the size of one pixel

$$PS = \frac{40.4 \,\mu\text{m}}{5.3 \,\mu\text{m}} = 7.63 \approx 7, \tag{25}$$

and according to this equation, the pixel sampling is 7x7. The total lenslet box size is 28x28 pixels, and this is calculated by dividing the $d_{lenslet}$ with D_{spot}. In this case, it is important that the spot size is clearly smaller than lenslet size, so the spots are not overlapped and the spots can be clearly distinguished.

5.3 Calculation of the wavefronts

Wavefront coefficents

Wavefronts are measured using the CIAO Python software [82]. The wavefronts measurements are based on the Zernike polynomials. Polar coordinates are the most common way to represent different aberrations, but Cartesian coordinates are used in this case because the shape of the sensor is square. The process of wavefront measurements with SHWFS consists of two parts: wavefront slope acquisition and wavefront reconstruction. The slope of the wavefront tells the displacement of the measured point from the optimal point and is calculated with the help of partial derivatives [83]. The partial derivatives of the x and y directions are a crucial part of the wavefront calculation, as shown in Equations 26 and 27

$$\frac{\Delta x(x,y)}{f} = \sum_j c_j \frac{\partial h_j(x,y)}{\partial x} \tag{26}$$

$$\frac{\Delta y(x,y)}{f} = \sum_j c_j \frac{\partial h_j(x,y)}{\partial y}, \tag{27}$$

where Δx is the slope change in the x direction, Δy is the slope change in y direction and f is the focal length of the lenslets, c_j is Zernike coefficient and h_j is the height. Figure 26 shows how the slope is related to displacement. The displacement is positive if the wavefront is behind the reference and negative if the wavefront is ahead of the reference wavefront.

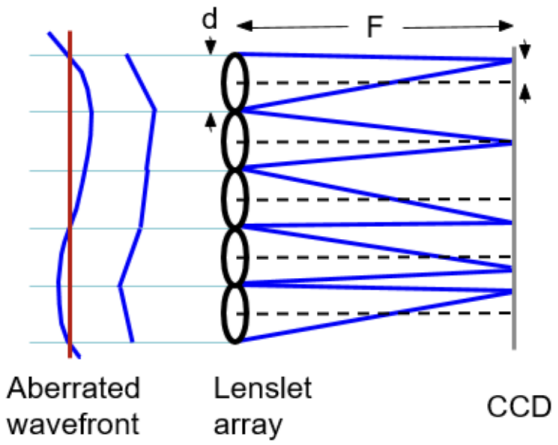

Figure 26: In the case of aberrated wavefront the spots are not focused in the reference point. The slope of the wavefront indicate the displacement of the spot. If the wavefront is behind the reference wavefront the displacement is positive and negative in case of preceding wavefront in vertical axis.

Partial derivatives can also be presented in the matrix form, as shown in Equation 28

$$G = FA, \tag{28}$$

where G is a gradient vector, corresponding partial derivatives, F is the wavefront reconstruction matrix, and A is the coefficent vector for Zernike polynomials. The coefficient matrix of Zernike polynomial can be calculated with Equation 29

$$A = F^{+}G, \tag{29}$$

where F^{+} is the pseudoinverse of matrix F [83].

The root-mean square (RMS) is strongly related to Zernike coefficients, as shown in Equation 30

$$RMS = \sqrt{\sum_{n>1,all\ m} (c_n^m)^2} \tag{30}$$

where c_m^n describes the Zernike coefficients. The n describes the total degree of the Zernike polynomial. The values n=0 and n=1 are ignored because they do not affect the quality of the image, as discussed in Chapter 3. It is also important to know that these coefficients change if the size of the pupil changes. The change is not easy, and the comparison between coefficients with different pupil sizes is not valid [12]. The Zernike coefficients are also related to calculation of the wavefronts. Wavefront W(x,y) is a linear combination of all Zernike polynomials, as shown in Equation 31

$$W(x,y) = \sum_{j}^{n} c_j Z_j(x,y) \tag{31}$$

where c_j describes the coefficent of Zernike polynomial and n the number of Zernike polynomials.

Dynamic range

A dynamic range is also an important factor that must be taken into account. The dynamic range describes the largest angle at which the spots can be measured accurately. In other words, it tells what are the measurements limits. The dynamic range can be calculated with Equation 32

$$\theta_{max} = \frac{\Delta s_{max}}{f} = \frac{d/2}{f}, \tag{32}$$

where Δs_{max} is the maximum displacement of the spot, d is the diameter of the lenslet, and f is the focal length of the lenslet [3]. In Equation 33, dynamic range is calculated

$$\theta_{max} = \frac{150 \cdot 10^{-6}\ \mathrm{m}}{2 \cdot 5.6 \cdot 10^{-3}\ \mathrm{m}} = 0.013\,39\,\mathrm{rad} \approx 0.77^\circ, \tag{33}$$

where the lenslet diameter is 150 µm and the focal length is 5.6 mm. In addition, this is expressed as dioptres, as shown in Equation 34

$$D_{max} = \frac{0.01339\ rad}{4.2\ mm} = 3.19\ D. \tag{34}$$

Sensitivity

The second important parameter is sensitivity. It tells which is the smallest detectable change. The sensitivity can be calculated using Equation 35,

$$\theta_{min} = \frac{\Delta s_{min}}{F}, \tag{35}$$

where Δs_{min} is the minimum spot displacement that can be detected and F is the focal length. The minimum spot displacement is dependent on the pixel size of the detector and the accuracy of centroid algorithm [3]. In this case, the CMOS pixel is used as Δs_{min} value. The Δs_{min} is calculated in Equation 36

$$\theta_{min} = \frac{\Delta s_{min}}{F} = \frac{5.3 \cdot 10^{-6}\ m}{4.2 \cdot 10^{-3}\ m} = 0.000946\ rad = 0.23\ D, \tag{36}$$

where θ_{min} can be converted to dioptres ($0.23\,\mathrm{m}^{-1}$). The dynamic range and sensitivity are linked to each other. The dynamic range is larger if the focal length is short, but the sensitivity weakens at the same time. Conversely, when the focal length is longer, the sensitivity improves but the dynamic range is reduced.

5.4 Testing protocol

To test the aberrometer, imaging protocol is divided into two parts. The first part is to plan a model eyes and take images of it. The second part is to use trial lenses and measure their aberrations.

In the case of model eyes, the settings require more components after the beam-splitter. The model eye consisted of three major components: the artificial retina (paper), iris diaphragm (aperture), and lens 3(achromatic doublet, f= 50mm). To give us more degrees of freedom in alignment, the artificial retina was mounted on a kinematic mount with tip/tilt adjustability to maximize the back-scattering signal in the WFS.

The first part is the cage system iris diaphragm, which adjusts the size of light that hits the pupil plane and reflects backward. The size of incoming light should be as similar as possible compared to the normal pupil size. After the iris diaphragm, the light travels to lens 3 which has a focal length of 50 mm. This focuses the light on the piece of paper which is attached to the aluminum mirror. The purpose of a piece of paper is to mimic the real eye. This mirror is inside the kinematic mount which has the possibility to tip or tilt this mirror. The single axis translation stage is used to adjust the mirror location in a horizontal direction. The model eye part is attached to the pedestal post which is inside the post holder. Information about the models and manufacturers of each component is shown in Table VII in Appendix.

The model eye was first used to measure the spot sizes created by the back-scattered light. Then different sensor exposure times where used to determine what is the signal-to-noise ratio (how much unwanted light scattering reaches the sensor in the dark). Finally, trial lenses with known aberrations (defocus aberrations) were placed near the pupil plane of the model eye to induce aberrations on the beam path which were recorded with the aberrometer using Python-based custom-software.

6 Technical performance

6.1 3D-modeling

6.1.1 Aberrometer

Aberrometer is drawn with Fusion 360, as seen in Figure 27. The main components of the aberrometer are marked as follows: 1) diode laser 2) camera 3) XY translating mount 4) beamsplitter. It is important to notice that the camera locates inside the sensor protector. The components for this system were exported from Thorlabs website. This made it easier to sketch how the off-to-shelf components fit to the optical system.

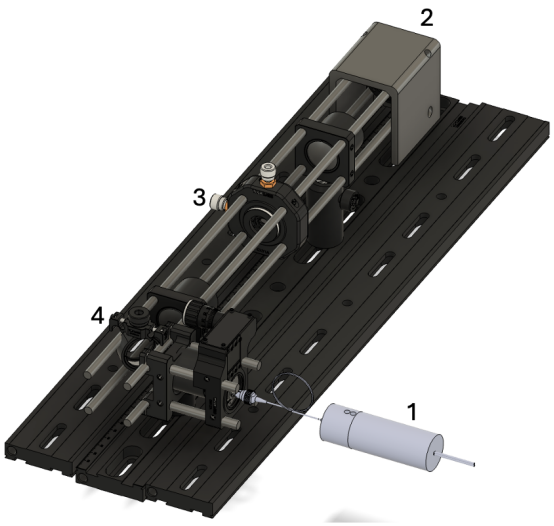

Figure 27: Aberrometer drawn in Fusion360 with components from Thorlabs. The numbers tell about the location of the following components: 1) diode laser 2) camera 3) XY translating lens mount 4) beamsplitter.

6.1.2 Trial lens holder

The trial lens holder was also modeled with the help of Fusion360. This was modeled because the trial lenses are too large to fit inside the cage rods. There is a groove in the middle of the trial lens holder that enables light transmission through the optical

center of the trial lens. The trial lens holder is also identical from the back and front, making it possible to attach to the rods. Figure 28 shows the trial lens from three different views. The location of the trial lens holder is before the beamsplitter.

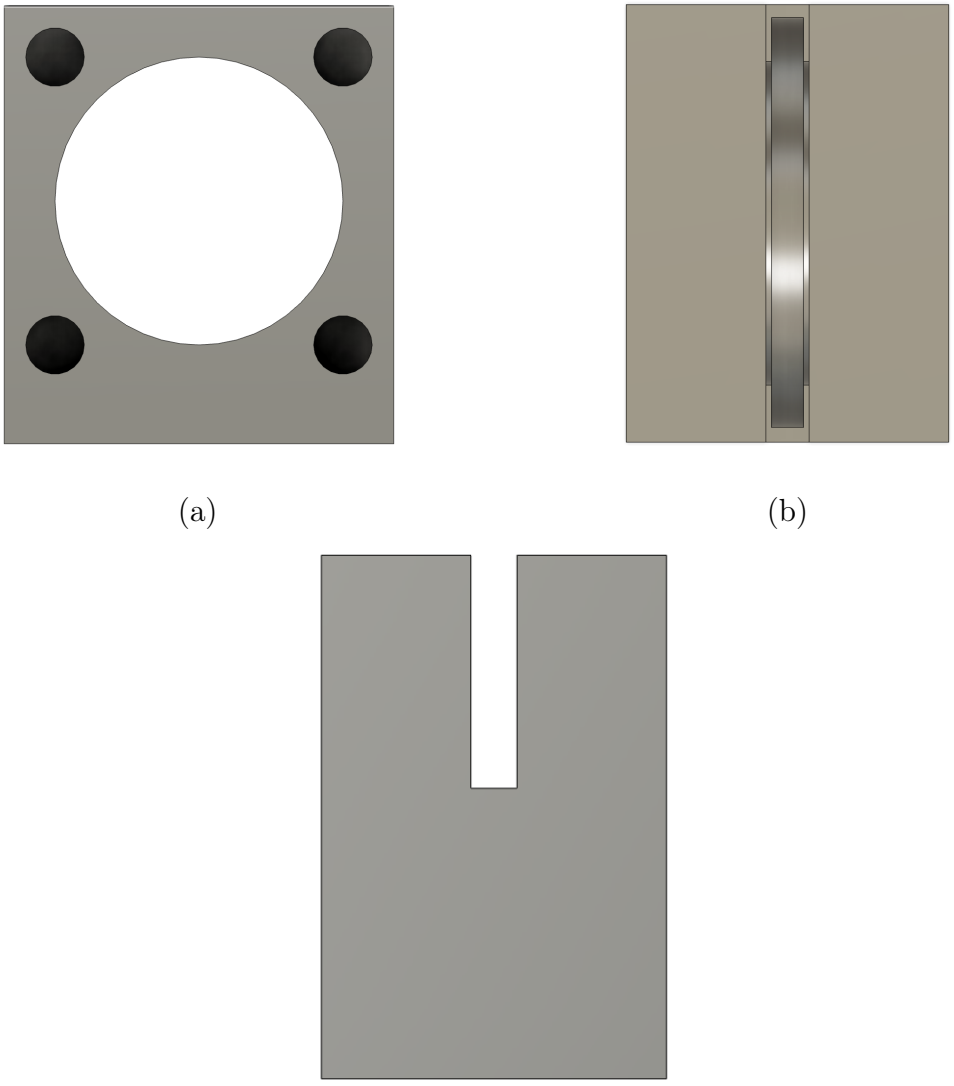

(a) (b)

(c)

Figure 28: a) This image shows the front view of the trial lens holder. b) Trial lens holder has a groove in the middle, which is where the trial lenses are placed. c) The side view of the trial lens holder.

The dimensions of the trial lens holder are shown in Figure 29. It shows the dimensions in the front view (a) and from the right side (b). The front view and back view are identical as are the right and the left views.

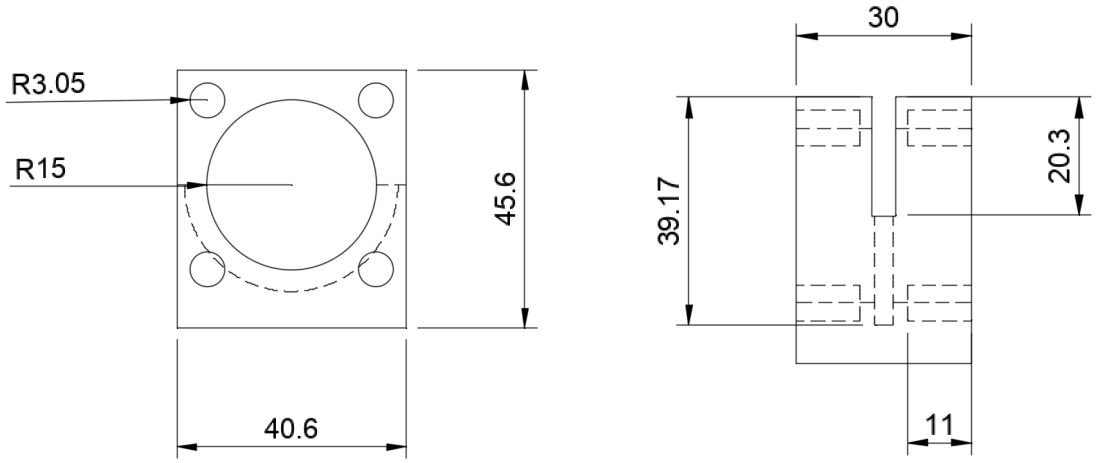

(a) (b)

Figure 29: a) The dimensions from the front view of the trial lens holder are shown with mm unit. b) The dimensions in right side view of the trial lens holder are shown with mm unit.

6.1.3 WFS enclosure

WFS enclosure was modeled to reduce the amount of reflected light to reach the sensor. The aim was that only light from the optical axis can reach the sensor and light from the screens of the devices like the computer and from environment can be excluded. WFS enclosure is placed from above. When reflections of light are excluded the Signal-to-noise ratio (SNR) is improved and the quality of the spots gets better. Figure 30 shows the WFS enclosure from three different views: front, bottom and left side. In addition, Figure 31 shows the size of the WFS enclosure from different points of views.

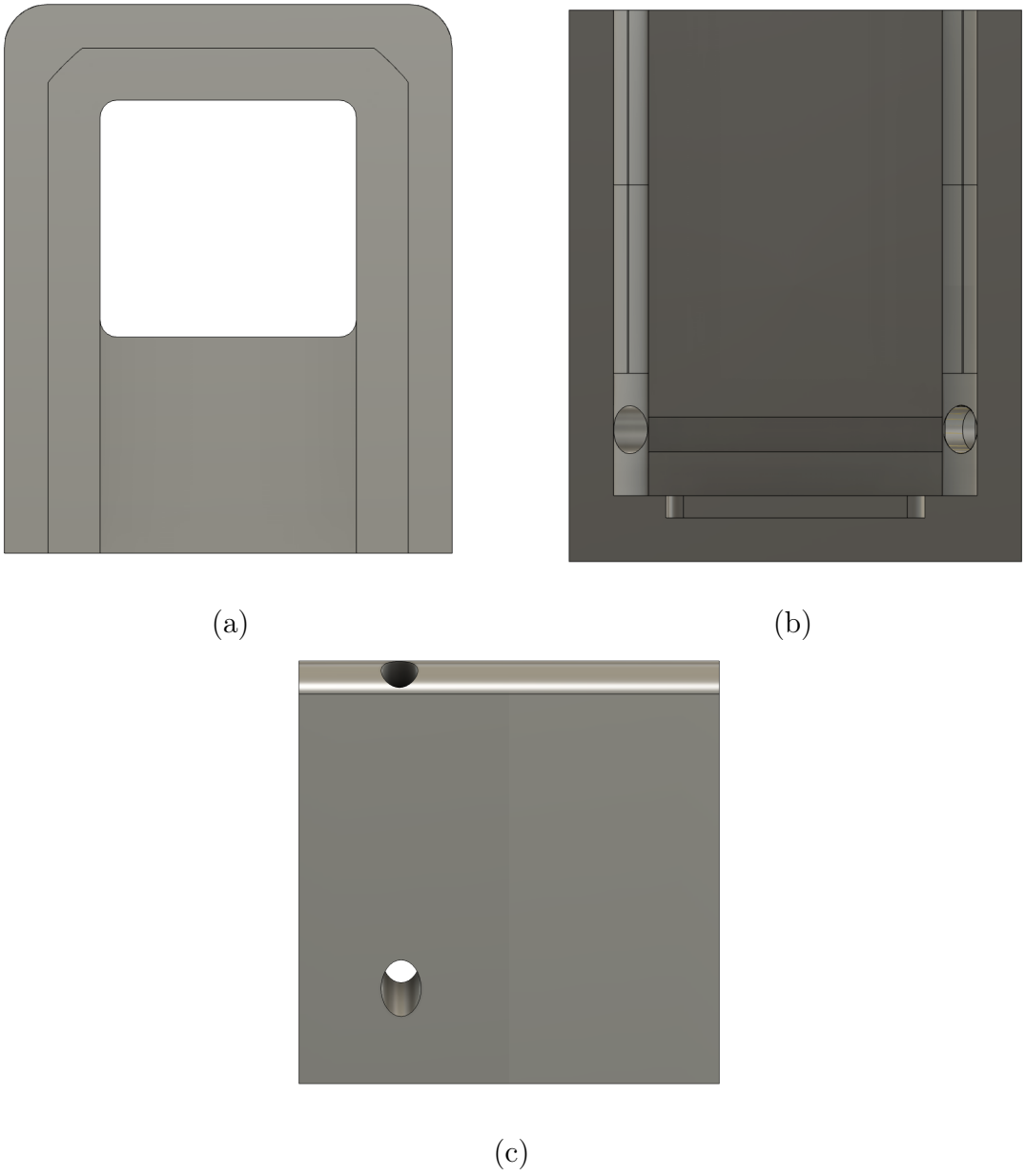

(a) (b)

(c)

Figure 30: a) WFS enclosure is shown from the front view. b) WFS enclosure is shown from the bottom. c) WFS enclosure is shown from the left side.

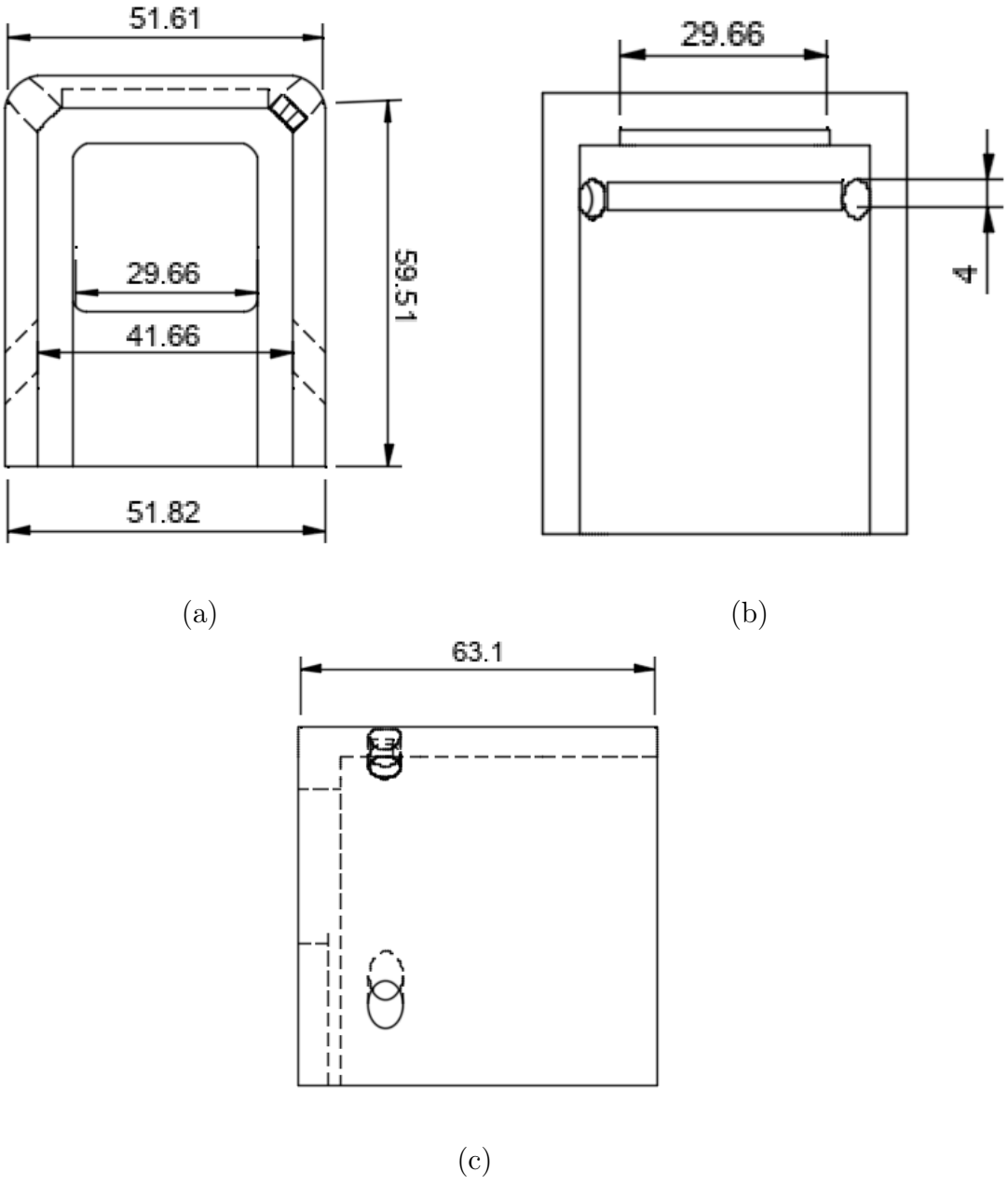

Figure 31: a) The dimensions of WFS enclosure are shown with mm from the front view. b) The dimensions of WFS enclosure are shown with mm unit from the bottom. c) The dimension of WFS enclosure is shown with mm unit from the left side.

6.2 Illumination

6.2.1 Quality of laser diode

The first thing to do was measure the power of the spectrum of the laser diode. The spectrum was measured with a spectrometer and it was measured with two different situations. The first measurement was made for the light that is transmitted outward to the aberrometer. In the second case, the light was directed in oblique angle to the spectrometer. This was executed by adding a oblique mirror between the beamsplitter and the model/real eye. Figure 32 shows the formed spectrum with laser diode.

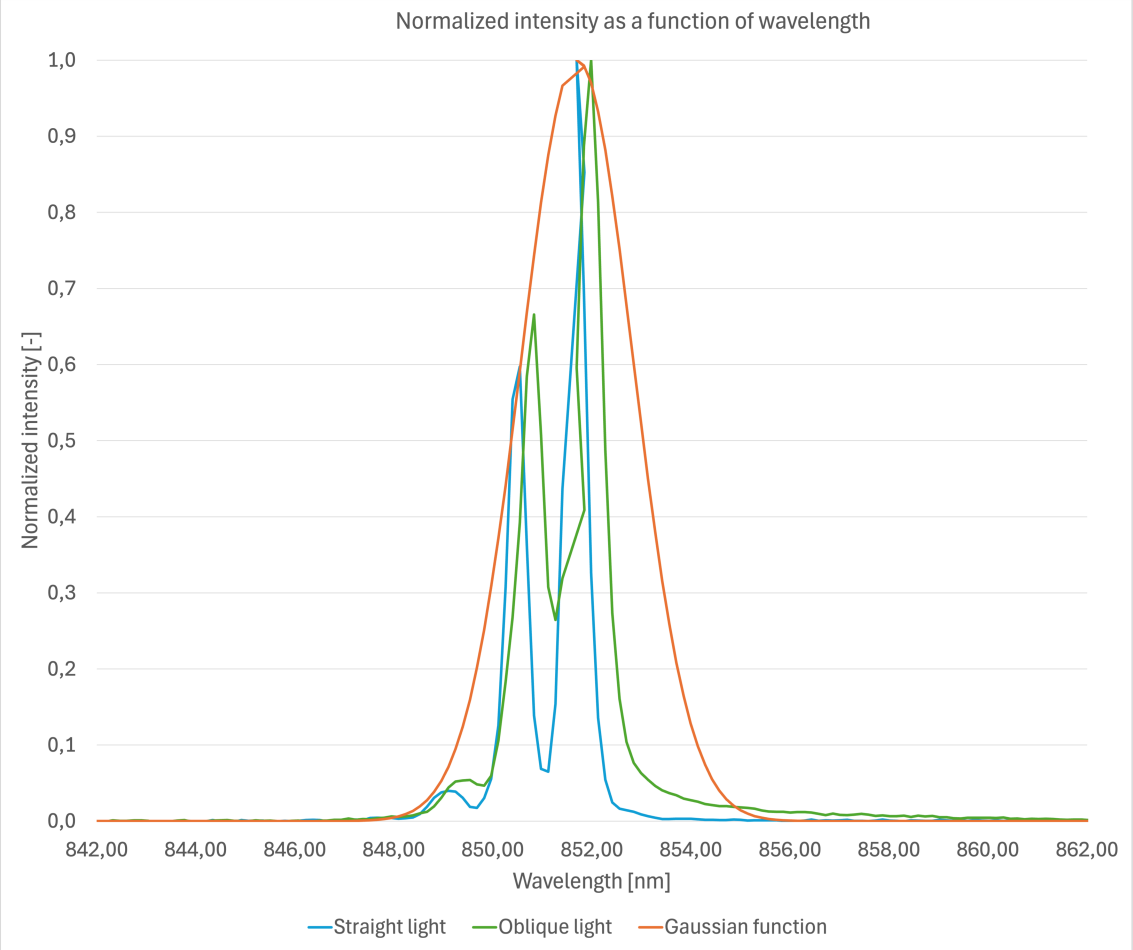

Figure 32: The spectrum of the laser diode is shown as a function of the wavelength. The blue curve shows the spectrum of straight light and the green curve shows the curve of the oblique light. Both of the curves have two peaks almost at the same point. The wavelength of the laser diode is 850±10nm, so both peaks are inside this error limit. In addition, Gaussian function is plotted to the same graph. The Gaussian function is $e^{\frac{(\lambda-851.7)^2}{(2\cdot 0.8)^2}}$.

The blue line describes the straight light and the green line describes the oblique light. The orange line describes gaussian function which is also shown in Equation 38

$$\psi(\lambda) = Ae^{\frac{(\lambda-\lambda_0)^2}{(2\sigma)^2}} \tag{37}$$

where ψ is gaussian distribution, λ is wavelength, A is amplitude, and λ_0 is the average of the two peaks and σ is parameter for the width of the beam. This parameter is determined with the help of FWHM because $\sigma = \frac{FWHM}{2 \cdot ln(2)}$. In this case, the data is normalized, so both straight and oblique light have 1 as a maximum value.

6.2.2 Effect of neutral density filters

The power of this laser beam after the beamsplitter is 2.05 mW. This means that it must be attenuated with the help of a neutral density filter (ND filter). The unit of attenuation is the optical density (OD). The higher the OD value, the greater the attenuation of the beam power. Different ND filters were attached to this system, and the smallest possible OD value when the power is below 0.75 mW is with 0.6 OD. The value with 0.6 OD is 0.649 mW. In practice, the attenuation must be at least 0.6 OD or higher.

The beamsplitter of this aberrometer is 90:10 which means that it lets 90 % of the light to pass and reflects 10% of the light. The reflected and transmitted light was measured with ND attenuation of 0.6, 0.7 and 0.8 OD. The results are shown in Table II. Approximately 90 % of the light transmit or reflect from the beamsplitter and the rest of the light is absorbed in the beamsplitter.

Table II: The powers of laser beam with 0.6, 0.7 and 0.8 OD are shown in this table. The power of laser is attenuated due to the ND filters. The percent value next to the power value tells how large part of the power of the light is measured in that spot. About 5 % of the light is reflected and about 85 % is transmitted.

OD	Power before beamsplitter	Reflectance power	transmittance power
0.6	12.77 mW	0.68 mW/5.3 %	11.01 mW/86.2%
0.7	10.31 mW	0.55 mW/5.3 %	8.66 mW/84.0 %
0.8	7.85 mW	0.45 mW/5.7 %	6.72 mW/85.6 %

The power of reflected light from the beamsplitter is 2.05 mW, so we can calculate the theoretical transmission values with Equation 14 and compare them to experimental results. Figure 33 shows the transmission of different OD values as a function of wavelength. Table III shows the experimental results with OD values 0.6, 0.7 and 0.8. The experimental and theoretical results are very close to each other, so the ND filters are working reliably.

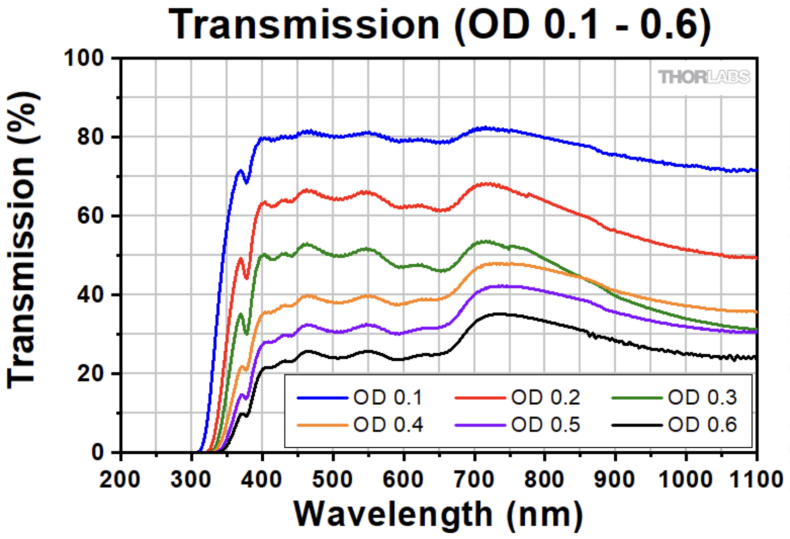

Figure 33: This image is copied from Thorlabs website [84] and this shows how large transmission is with different ND filter and wavelengths.

Table III: Experimental and theoretical results are shown for three OD values. Theoretical value for 0.6 OD can be straightly seen in Figure 33. Theoretical value for 0.7 OD is calculated by multiplying the 0.6 OD transmission percent with 0.1 OD transmission percent and, similarly, 0.8 OD by multiplying 0.6 OD with 0.2 OD.

OD	Experimental	Theoretical
0.6	31.6 %	31.2 %
0.7	24.7 %	24.4 %
0.8	19.0 %	18.8 %

6.3 Model eye

6.3.1 Quantifying the SHWFS spot quality

In this section, 10 different images were taken in addition to the background image. This was performed using the Ximea software. Pinhole between the two lenses was not able to suppress all the reflections coming from the model eye lens and therefore the background image was taken by blocking the beam entering the artificial retina. The exposure time was 3 ms and was constant in every image. The only difference between the images was made by editing the tip/tilt settings.

Figure 34 shows an example of how the real signal was measured. The background signal was subtracted from the measured signal and the real signal is achieved. This was done using Fiji software (version 2.16.0).

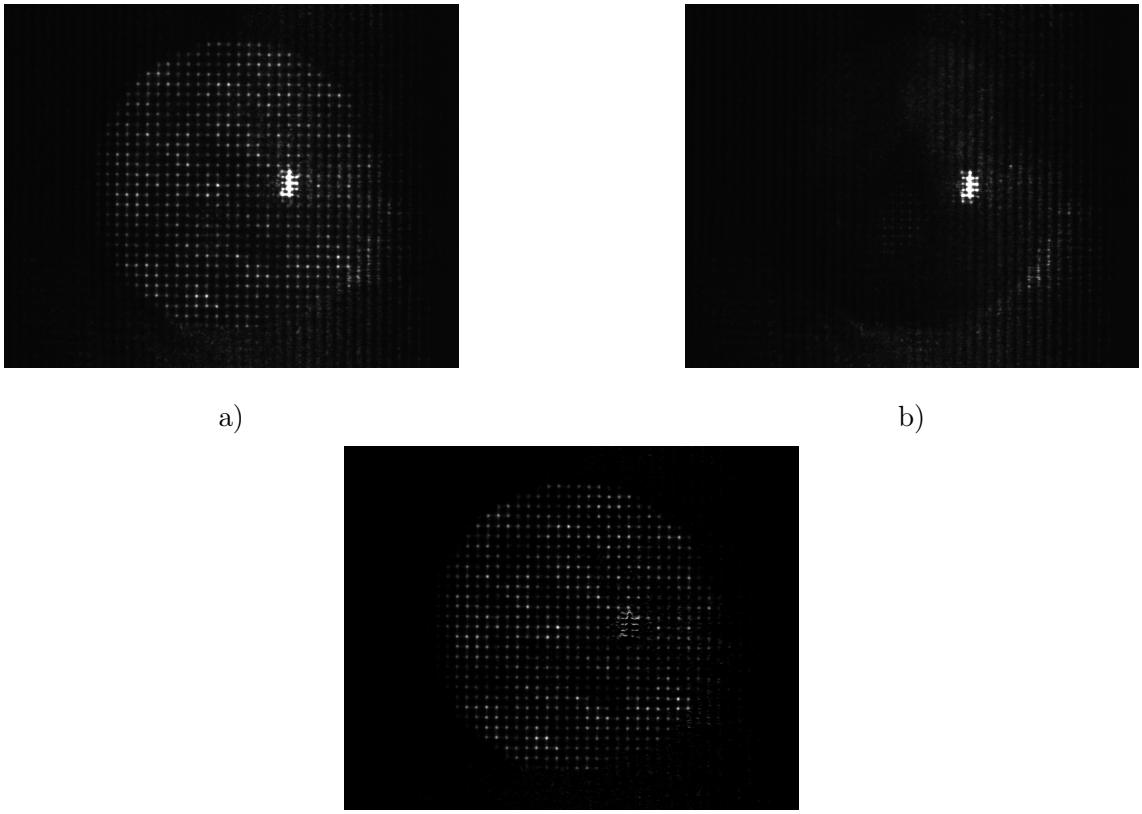

a) b)

c)

Figure 34: a) This image shows the real image of measured model eye. In this case, the light was directed to the model eye and reflected back to the sensor. b) The pass of the light was inhibited to the model eye by black barrier. This tells the magnitude of the signal coming from the aberrometer itself, so this give the data of the background signal. c) The background signal is subtracted from the measured signal, yielding the real signal without background.

Two different spots are analyzed. Figure 35 shows the image of both spots and their gray values as a function of distance. The uppermost images show the real image of the spots. The unit of the distance is the pixel, and the second image shows this function vertically and the third horizontally. Gaussian function is shown in Equation 38

$$y = A \cdot e^{\frac{(x-x_O)^2}{2.355 \cdot \sigma^2}} \tag{38}$$

where A is the amplitude, x_o is the location of the amplitude and σ is the standard deviation. This is fitted for the measurement points. The FWHM can be solved by using the standard deviation value, as shown in Equation 39.

$$FWHM = 2.355 \cdot \sigma \tag{39}$$

where $FWHM$ is the full width at half maximum and σ is the standard deviation. The standard deviation varies between 3.2 and 3.3, giving FWHM values between 7.54 and 7.77 pixels. The real size of the spot can be calculated by multiplying the FWHM value by the size of one pixel. Because the size of one pixel is 5.3 µm, it means that the FWHM is between 39.94-41.19 µm. This is very close to the size calculated in Equation 24 (40.4µm). Because the magnification of the aberrometer is 0.329, it means that the FWHM is between 13.15-13.55 µm in the model eye. By using Equation 10, it is possible to calculate the focal length of the model eye, as shown in Equation 40

$$f = \frac{D_f \pi D_c}{4\lambda} = \frac{13.2\,\mu m \cdot \pi \cdot 4.2 \cdot 10^{-3}\ m}{4 \cdot 850 \cdot 10^{-9}\ m} = 51.7\ mm. \tag{40}$$

Another possible parameter for the diameter of the beam is $1/e^2$. The parameter value $1/e^2$ can be multiplied with the amplitude value and after that it can finally replace the parameter y, making it possible to solve two different values of x. The difference between these values is the diameter of the beam. The parameter $1/e^2$ varies between 12.8-13.2 pixels (67.90-70.00 µm). All FWHM and $1/e^2$ results are shown in Table IV.

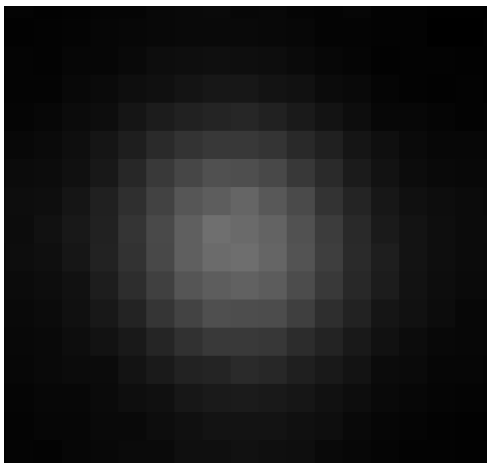

(a) Spot 1

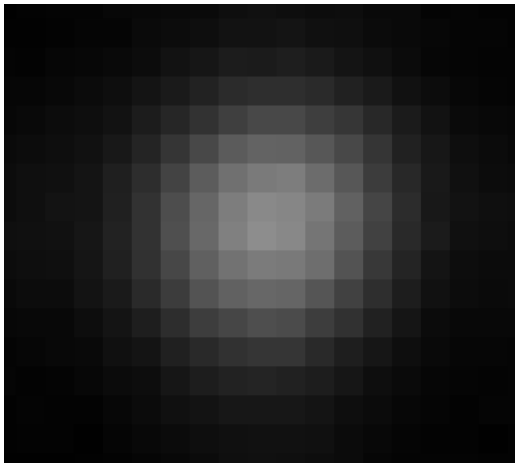

(b) Spot 2

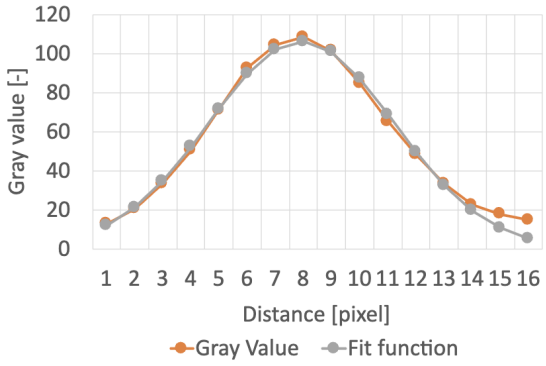

(c) Spot 1 vertical direction with fit function $y = 108 \cdot e^{-\frac{(x-6.93)^2}{2 \cdot 3.3^2}}$

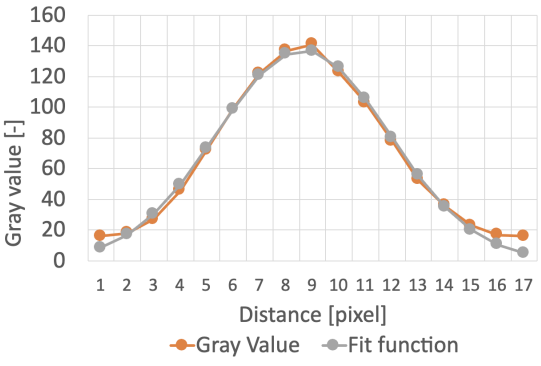

(d) Spot 2 vertical direction with fit function $y = 137.37 \cdot e^{-\frac{(x-7.64)^2}{2 \cdot 3.25^2}}$

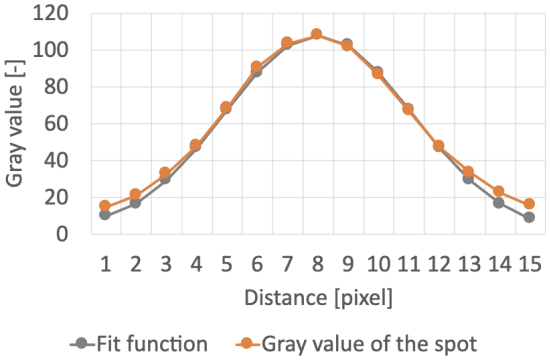

(e) Spot 1 horizontal direction with fit function $y = 108 \cdot e^{-\frac{(x-7.00)^2}{2 \cdot 3.2^2}}$

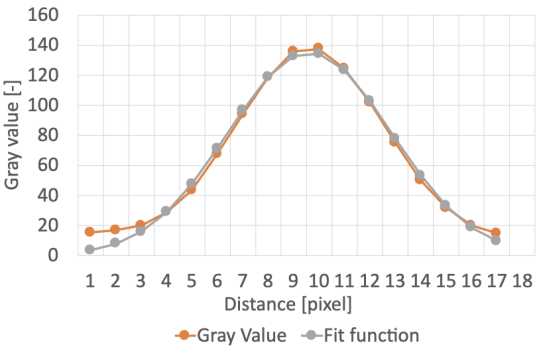

(f) Spot 2 horizontal direction with fit function $y = 135.19 \cdot e^{-\frac{(x-8.63)^2}{2 \cdot 3.2^2}}$

Figure 35: The gray values of two spots are shown as a function of distance. The orange line describes the fit function and the grey line describes the Gaussian fit function.

Spot number and direction	FWHM [μm]	$1/e^2$[μm]
spot 1 horizontal	39.94	67.90
spot 1 vertical	41.19	70.00
spot 2 horizontal	40.58	67.90
spot 2 vertical	40.58	68.97

Table IV: FWHM and $1/e^2$ values for spot 1 and 2 are shown in horizontal and vertical directions. Both of these parameters can be used for determining the beam diameter. FWHM is 50 % of the intensity maximum and $1/e^2$ is 13.5 %.

6.3.2 Signal-to-noise ratio

Signal-to-noise ratio (SNR) is determined to find out the noise which is reflected from the components and environment to the sensor. SNR can be calculated in two different ways. The first way is shown in Equation 41

$$SNR = \frac{P_{signal}}{P_{noise}}, \tag{41}$$

where P_{signal} describes the power of the signal and P_{noise} describes the power of the noise. The second way is to use Equation 42

$$SNR = \frac{\mu}{\sigma}, \tag{42}$$

where μ is the mean of the signal and σ is the standard deviation of the noise.

The SNR calculations are performed with ImageJ software. Exposure times between 1-3 ms with 0.25 ms gaps are used. With every exposure time, the normal spot image and the background image are taken. The background image is taken by inhibiting the light to receive the model eye. similarly to the previous chapter. The background image is subtracted from the normal image.

The results of Equations 41 and 42 are shown in Figure 36. The best value of SNR is applied with 2.50 ms exposure time.

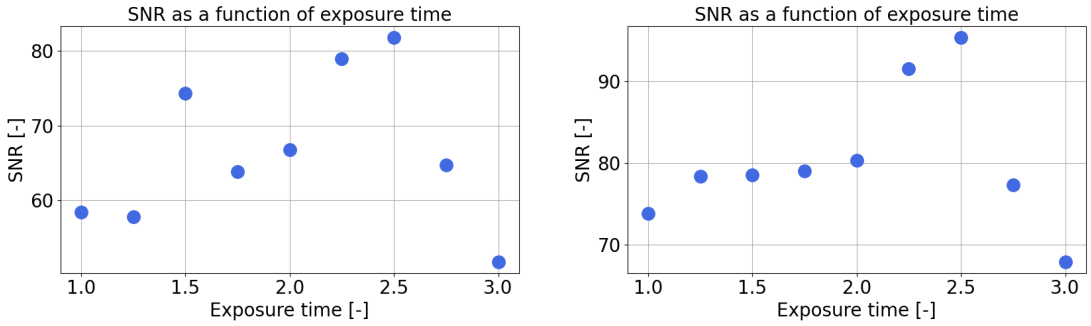

(a) (b)

Figure 36: a) SNR is shown as a function of exposure time and SNR is calculated with Equation 41. With exposure time 2.50 ms, the best possible SNR is applied. b) SNR is shown as a function of exposure time and SNR is calculated with Equation 42. Similarly than previous case, the best possible SNR is applied with 2.50 ms.

6.4 Trial lenses

The wavefronts of eight different trial lenses were measured. The diopter values of the trial lenses ranged from -1 D to 1D with 0.25 D gaps and without 0 D measurements. Trial lenses cause defocus aberration. The wavefronts were reconstructed with Python with data of the x- and y-slopes. In the beginning, the reference plane was first made as flat as possible. The flattest situation was achieved with defocus 76 nm, astigmatism 0 degree 8.5nm, and astigmatism 45 degree 34 nm with a root mean square error (RMSE) value of about 100 nm. RMSE is used as a parameter for residual wavefront error [85]. Figure 37 shows wavefront measurements with negative trial lenses and Figure 38 shows the Zernike coefficients of measurements. For positive lenses, Figure 39 shows results from wavefront measurements and Figure 40 results of Zernike coefficients.

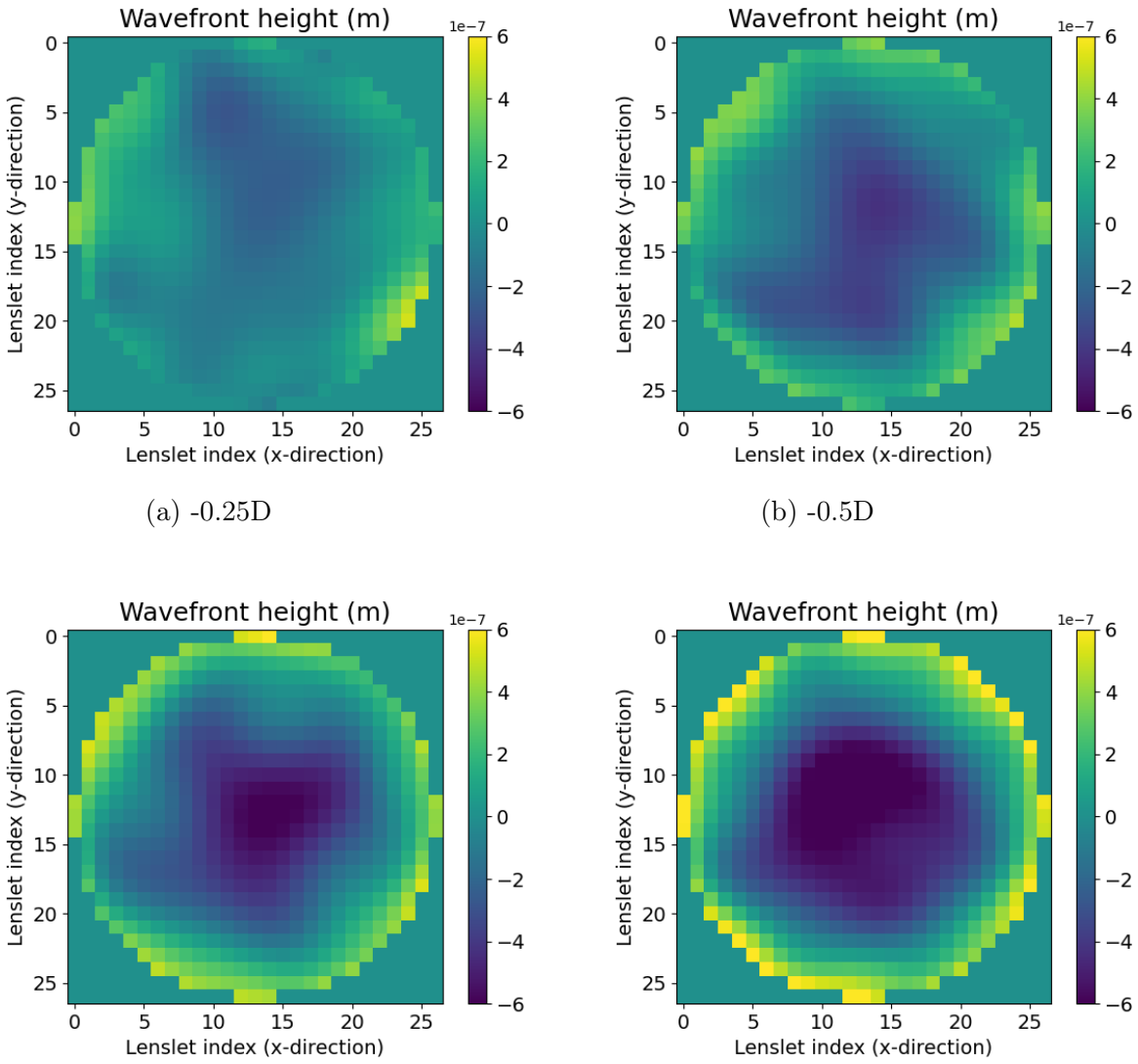

(a) -0.25D

(b) -0.5D

(c) -0.75D

(d) -1.0D

Figure 37: All four wavefront measured with negative dioptre lenses are shown.

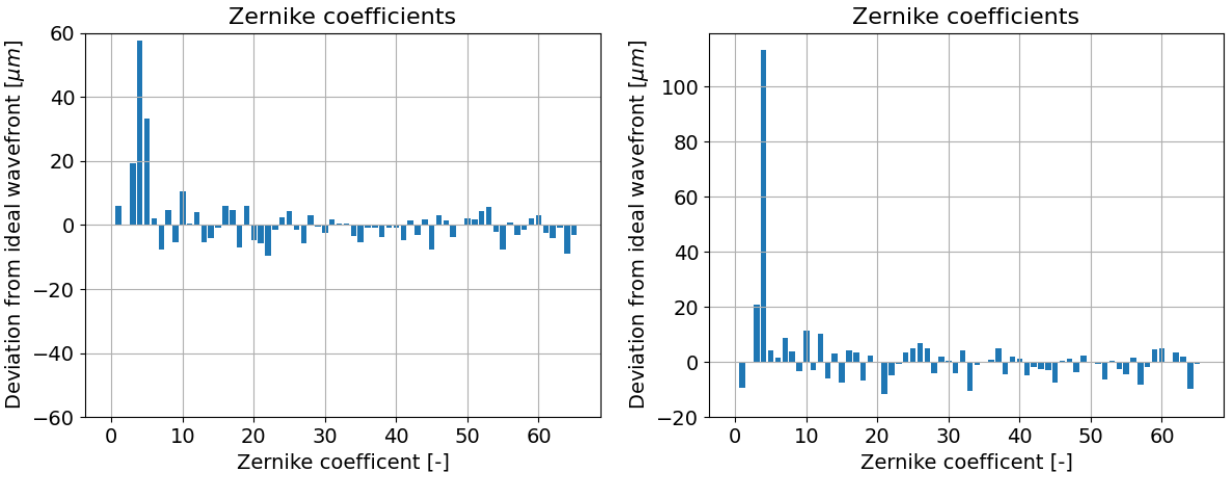

(a) -0.25D

(b) -0.5D

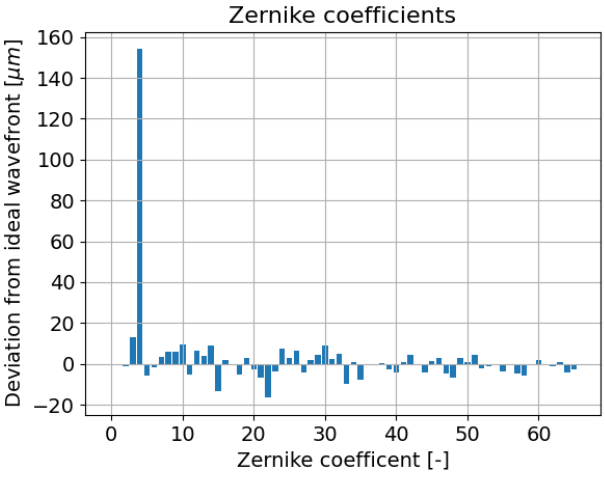

(c) -0.75D

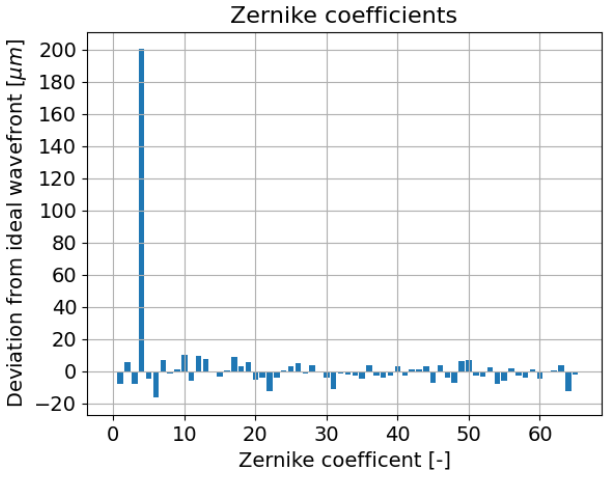

(d) -1.0D

Figure 38: The wavefront coefficients of all four wavefronts with negative diopter lenses are shown. Positive lenses refract light weaker than neutral lenses, which causes the wavefronts to fall behind the ideal wavefront. As a result, this leads to a positive defocus aberration.

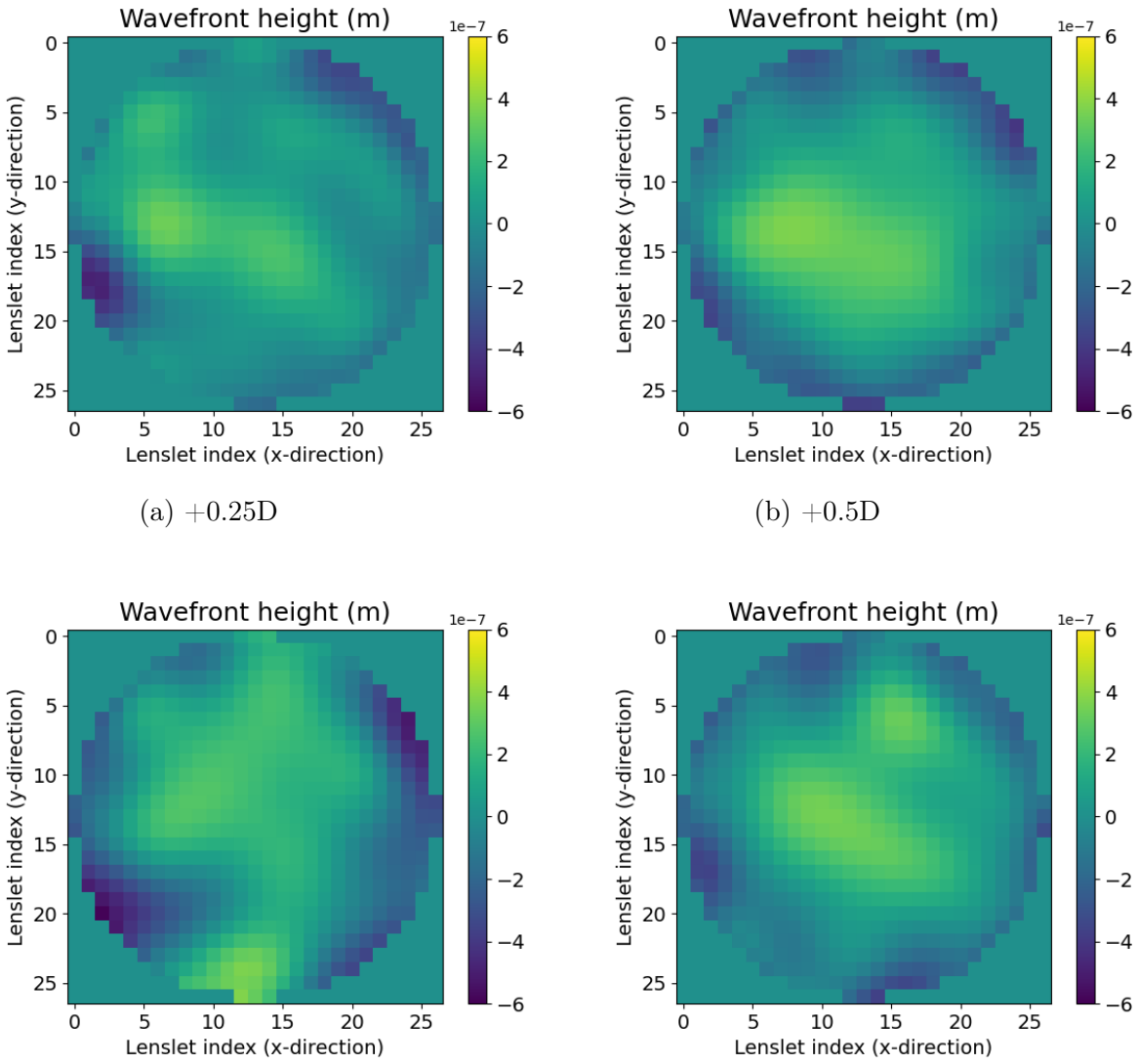

(a) +0.25D

(b) +0.5D

(c) +0.75D

(d) +1.0D

Figure 39: All four wavefronts measured with positive dioptre lenses are shown. Negative values are shown in bluish colors, and positive values in yellowish colors. With more negative dioptre values, the slopes become steeper.

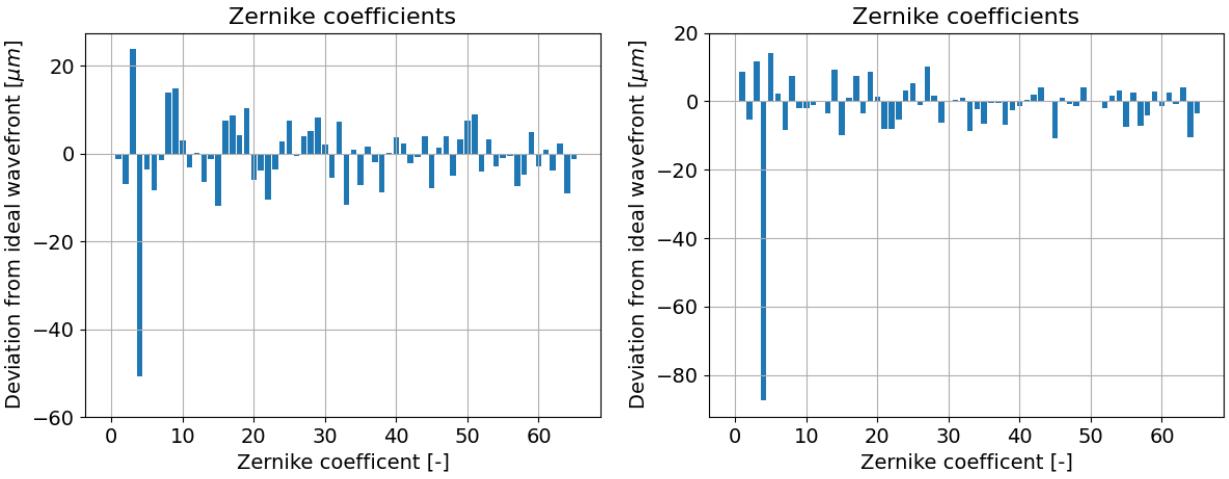

(a) -0.25D

(b) -0.5D

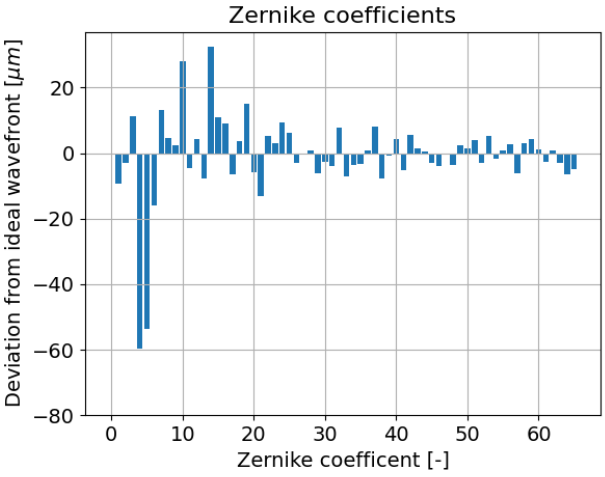

(c) -0.75D

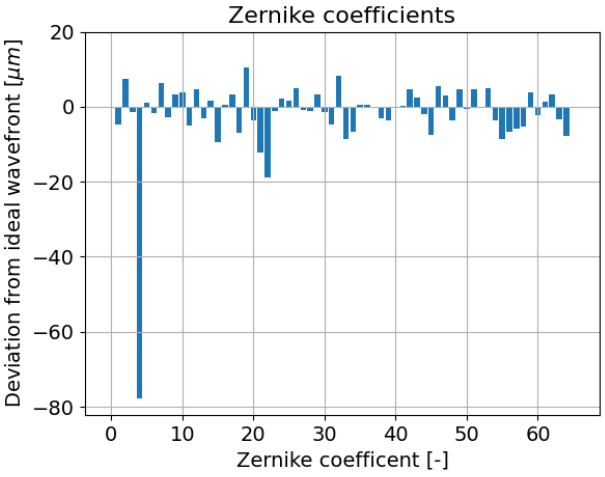

(d) -1.0D

Figure 40: The wavefront coefficients of all four wavefronts with positive diopter lenses are shown. Positive lenses refract light more strongly than neutral lenses, which causes the wavefronts to fall in front of the ideal wavefront. As a result, this leads to a negative defocus aberration.

7 Discussion

This aberrometer was built of off-the-shelf and self-designed components which resulted in large reduction in costs with the total cost of the system being roughly one-third of the price for commercial SH-WFS . The components were bought from Thorlabs, except for CMOS which was bought from Ximea, and CIAO software was used for measurements. In addition to purchased components, specialized parts were designed with Fusion 360 and 3D-printed in-house. After calculating the theoretical parameters and selecting suitable components for the optical design, the system was physically modeled in Fusion 360 to validate the dimensions of opto-mechanics and made sure that it was feasible to build. Once built, key components such as the light source, filters, beam-splitter and image sensor went through performance testing. Finally, wavefront map and Zernike coefficients are measured with trial lenses to see the feasibility for aberration measurements.

The measurements and calculations matched with each other quite well. For example, the FWHM value was calculated to be between 39.96-41.18 µm and the calculations gave 40.4 µm. The variation between the FWHM is due to the imperfect collimation and alignment. However, the variation was only 1.2 µm so it is negligible. With Equation 40, the model eye focal length was calculated to be 51.7 mm, which is very close to the focal length of Lens 3 (50 mm). Due to these factors, the theory and experimental results are in good agreement.

The trial lenses with negative diopter values gave reasonable results according to wavefront maps and wavefront coefficients. However, trial lenses with positive diopter values gave much worse results. The trial lens position might not have been optimal and the mount allowed some tip/tilt. For future research, the mount should be redesigned based on these results and potentially coupled to optomechanics for more accurate control. The other Zernike coefficients were consistently small, which means that performance is repeatable. On the other hand, other Zernike coefficients

besides defocus prove that the reference wavefront is not flat. Good repeability is also achieved with other aberrometers [83]. Compared to other Shack-Hartmann wavefront maps, the values of the Zernike coefficients are in the same range [86].

The spectrum of the laser diode was measured with two angles. The spectrum had two peaks in both situations, but both peaks are within the error limit. The beamsplitter lets about 5% of the light to reflect and about 85% of the light to transmit. The beamsplitter is 90/10, so about 5% is missing from both directions, and this is probably due to the absorption and scattering of the beamsplitter. These reasons probably affect the laser diode results. The transmissions of neutral density filters match very well with theoretically calculated percentages.

The SNR was determined from the spot images and was determined in two ways. Both ways gave the same results, so with an exposure time of 2.5 ms the SNR gets its best value. This is very close to the exposure time (2.89 ms) used with time-resolved aberrometer and 3.9 mm pupil [2]. The reason why the two largest exposure times weaken the SNR is related to saturation. Saturation is also familiar with other studies related to aberrometers [87]. The tails of the spots often overlapped, which also increased the noise in the background. The RMSE value of the aberrometer was about 100nm (0.117λ). In comparison, the RMSE was 0.0496λ with an aberrometer that uses deep learning [85].

Despite the mainly reliable results, some problems were encountered during testing of this aberrometer. One of the main challenges was the reflections. Although antireflection coating was used with the model eye, it did not prevent all reflections. The reflections were also tried to remove by changing the positions of the beamsplitter and the pinhole and the distance of the model eye. The reflections were mainly eliminated by using the pinhole even though it is larger than theoretical calculations. The alignment of the pinhole was quite difficult because the Rayleigh range was only 18.8 µm. Another challenge was that the height of the laser beam was not similar

with different distances. For example, when measuring the laser height with light transmitted from beamsplitter, the height was a little bit different. This system had many degrees of freedom, which also made the situation even more difficult.

Overall, the study of this aberrometer was successful, except for measurements with positive test lenses. Using smaller pinhole and higher quality components are ways to improve this system and reduce reflections. The next steps are to build another detection path, attach it to this system and measure the aberrations from the real eye. For real eye measurements, permission from the Ethics Committee is required. It will tell more about the feasibility for determining the aberrations and comparison with expensive components will reveal more about the price-quality ratio of this aberrometer.

8 Conclusions

The aberrometer was built according to the theoretically calculated parameters and with off-to-shelf components. The measured light spot sizes and quality were consistent with theoretical expectations and this study pointed out that it is possible to measure aberrations of the eye with this aberrometer. However, the measurements of Zernike coefficients also indicate that the reference wavefront is not totally flat and that the trial lens mount is not optically perfectly aligned. The results were also consistent with other similar studies. This system is designed for potential research use and is used as a test platform for CIAO software when new properties are available.

References

[1] S. V. Badescu, R. Barac, S. Schmitzer, and C. Tataru, Romanian Journal of Ophthalmology **59**, 217 (2015).

[2] C.-E. Leroux, Time-resolved aberrometry of the eye with a Shack-Hartmann wavefront sensor, 2010, phD thesis.

[3] J. Porter *et al.*, *Adaptive Optics for Vision Science: Principles, Practices, Design, and Applications* (John Wiley Sons, Inc , 2006).

[4] J. Mompeán, J. L. Aragón, P. M. Prieto, and P. Artal, Future Generation Computer Systems **91**, 177 (2019).

[5] E. Brunner *et al.*, Biomedical Optics Express **12**, 5969 (2021).

[6] K.-N. Joo and H. M. Park, Current Optics Photonics **7**, 325 (2023).

[7] C. Rao *et al.*, PhotoniX **5**, 16 (2024).

[8] K. V. Vienola, D. Valente, R. J. Zawadzki, and R. S. Jonnal, Optica **9**, 1100 (2022).

[9] H. Hashemi *et al.*, Cornea **28**, 395 (2009).

[10] S. Galgauskas, G. Juodkaite, and J. Tutkuvienė, Clinical Interventions in Aging **9**, 1145 (2014).

[11] M. S. Sridhar, Indian Journal of Ophthalmology **66**, 190 (2018).

[12] D. A. Atchison and G. Smith, *Optics of the Human Eye*, 2nd ed. (CRC Press , 2023).

[13] J. H. Krachmer, M. J. Mannis, and E. J. Holland, *Cornea E-Book*, 5th ed. (Elsevier Health Sciences Philadelphia, 2016).

[14] R. Carlos de Oliveira and S. E. Wilson, Experimental Eye Research **197**, 108090 (2020).

[15] M. Kiel *et al.*, Journal of Ophthalmology **2022**, 9520512 (2022).

[16] M. Guillon *et al.*, Optometry and Vision Science **93**, 1093 (2016).

[17] S. Mathôt, Journal of Cognition **1**, 16 (2018).

[18] S. A. Kennedy, J. Noble, and A. M. Wong, Canadian Medical Association Journal **185**, E424 (2013).

[19] I. Rehman, B. Hazhirkarzar, and B. C. Patel, *Anatomy, Head and Neck, Eye* (StatPearls [Internet] Cornell University, Johns Hopkins, University of Utah, 2023), last update: July 24, 2023.

[20] X. Ruan, Z. Liu, L. Luo, and Y. Liu, BMJ Open Ophthalmology **5**, e000459 (2020).

[21] J. F. Hejtmancik and A. Shiels, Progress in Molecular Biology and Translational Science **134**, 119 (2015).

[22] B. D. Hood, B. Garner, and R. J. W. Truscott, Journal of Biological Chemistry **274**, 32547 (1999).

[23] M. V. Cicinelli *et al.*, The Lancet **401**, 377 (2023).

[24] S. Wagner, E. Zrenner, and T. Strasser, Vision Research **163**, 42 (2019).

[25] P. N. Bishop, Progress in Retinal and Eye Research **19**, 323 (2000).

[26] Z. Yao, Q.-Y. Gao, and Y.-N. Hui, International Journal of Ophthalmology **15**, 857 (2022).

[27] A. M. Paniagua-Diaz *et al.*, Investigative Ophthalmology & Visual Science **65**, 20 (2024).

[28] A. M. Rasys *et al.*, BioEssays (2023).

[29] AnatomyTool, Gallery - AnatomyTool, 2025, accessed: 2025-01-31.

[30] L. A. Ostrin *et al.*, Investigative Ophthalmology & Visual Science **64**, 4 (2023).

[31] F. L. Pedrotti, L. M. Pedrotti, and L. S. Pedrotti, in *Introduction to Optics* (Prentice Hall Englewood Cliffs, NJ, 1993), pp. 419–437.

[32] S. Kasthurirangan, E. L. Markwell, D. A. Atchison, and J. M. Pope, Investigative Ophthalmology Visual Science **49**, 2531 (2008).

[33] E. S. Enaholo, M. J. Musa, and M. Zeppieri, The Spherical Equivalent, 2024.

[34] U. Schiefer *et al.*, Deutsches Ärzteblatt International **113**, 693 (2016).

[35] M. U. R. Parrey and E. Elmorsy, Pakistan Journal of Medical Sciences **35**, 394 (2019).

[36] C.-W. Pan, D. Ramamurthy, and S.-M. Saw, Ophthalmic and Physiological Optics **31**, 3 (2011).

[37] H. Singh *et al.*, Indian Journal of Ophthalmology **70**, 2788 (2022).

[38] D. L. Mayer *et al.*, Jama Ophthalmology **119**, 1625 (2001).

[39] V. D. Castagno *et al.*, BMC Ophthalmology **14**, 163 (2014).

[40] M. Resan, M. Vukosavljeviæ, and M. Milivojeviæ, Advances in Ophthalmology 191 (2012).

[41] Wikimedia Commons contributors, Astigmatism2.svg, 2024, [Online; accessed 24-Jan-2025].

[42] S.-F. Mohammadi, M. Khorrami-Nejad, and M. Hamidirad, Clinical Optometry **11**, 85 (2019).

[43] T. A. Refai, Electron Physician **7**, 1296 (2015).

[44] N. B. Faal, H. Ojaghi, and S. S. Ahari, Journal of Current Ophthalmology **33**, 400 (2022).

[45] *Age-Related Changes of the Human Eye*, *Aging Medicine*, edited by C. A. P. Cavallotti and L. Cerulli (Springer Rome, Italy, 2008).

[46] S. Bentley *et al.*, Journal Patient Reported Outcomes **5**, 114 (2021).

[47] M. N. Miranda, Transactions of the American Ophthalmological Society **77**, 603 (1979).

[48] M. Romero-Jiménez, J. Santodomingo-Rubido, P. Flores-Rodríguez, and J.-M. González-Méijome, Journal of Optometry **8**, 48 (2014).

[49] Y.-J. Lai, S.-I. Yeh, and H.-C. Cheng, Taiwan Journal of Ophthalmology **5**, 72 (2015).

[50] *Customized Laser Vision Correction*, edited by M. M. Sinjab and A. B. Cummings (Springer International Publishing Cham, Switzerland, 2018), library of Congress Control Number: 2018942221.

[51] P. Artal *et al.*, Journal of Vision **4**, 4 (2004).

[52] M. M. Rodrigues *et al.*, Journal of Physics: Conference Series **1194**, 012093 (2019).

[53] M. V. Svechnikov, N. I. Chkhalo, M. N. Toropov, and N. N. Salashchenko, Optics Express **23**, 14677 (2015).

[54] K. Niu and C. Tian, Journal of Optics **24**, 123001 (2022).

[55] W. N. Charman, Journal of Cataract Refractive Surgery **28**, 75 (2005).

[56] J. M. Geary, *Introduction to Wavefront Sensors* (SPIE Press , 1995).

[57] A. L. Pettersson *et al.*, Contact Lens and Anterior Eye **31**, 189 (2008).

[58] R. Kingslake and R. B. Johnson, *Lens Design Fundamentals*, 2nd ed. (Elsevier Academic Press Amsterdam; Boston; Heidelberg; London; New York; Oxford; Paris; San Diego; San Francisco; Singapore; Sydney; Tokyo, 2010), co-published by SPIE, PM195.

[59] D. Azzam and Y. Ronquillo, Snellen Chart, 2023, statPearls [Internet].

[60] R. M. van den Berg *et al.*, Vision **6**, 76 (2022).

[61] L. Hervella, E. A. Villegas, P. M. Prieto, and P. Artal, Journal of Cataract & Refractive Surgery **45**, 87 (2019).

[62] J. Schwiegerling and D. R. Neal, in *Robert Shannon and Roland Shack: Legends in Applied Optics*, edited by J. E. Harvey and R. B. Hooker (SPIE Press Bellingham, WA, 2005), pp. 132–139.

[63] B. C. Platt and R. Shack, Journal of Refractive Surgery **17**, S573 (2001).

[64] R. von Fintel, Modern CMOS Cameras as Replacements for CCD Cameras, White Paper, Basler AG, 2018, accessed: 2024-10-23.

[65] R. von Fintel, Technical report, Baslerweb, (unpublished), accessed: 2025-03-04.

[66] K. M. Hampson *et al.*, Nature reviews. Methods primers **1**, 68 (2021).

[67] A. Burvall, E. Daly, S. R. Chamot, and C. Dainty, Optics Express **14**, 11925 (2006).

[68] R. K. Tyson, *Adaptive Optics Engineering Handbook* (Marcel Dekker, Inc. New York, NY, 2000).

[69] Y. Liu *et al.*, Nature Communications **15**, 10409 (2024).

[70] N. Doble, D. T. Miller, G. Yoon, and D. R. Williams, Applied Optics **46**, 4501 (2007).

[71] F. Rigaut, Publications of the Astronomical Society of the Pacific **127**, 1197 (2015).

[72] M. Aubailly and M. A. Vorontsov, in *Adaptive Optics Progress*, edited by R. K. Tyson (IntechOpen , 2012), p. N/A, open access.

[73] H. Ashourizadeh *et al.*, Diagnostics **13**, 2413 (2023).

[74] T.-C. Lim, S. Chattopadhyay, and U. R. Acharya, Medical Engineering & Physics **34**, 129 (2012).

[75] A. G. Podoleanu, Journal of Microscopy **247**, 209 (2012).

[76] F. J. Rodríguez, G. Staurenghi, and R. Gale, Graefes Archive for Clinical and Experimental Ophthalmology **256**, 2019 (2018).

[77] Louis Pressbooks, Appendix E: Water Properties, `https://louis.pressbooks.pub/chemistry1/back-matter/appendix-e-water-properties/`.

[78] E. Optics, Gaussian Beam Propagation, 2025, https://www.edmundoptics.com/knowledge-center/application-notes/lasers/gaussian-beam-propagation/.

[79] S. Ragland *et al.*, in *Point spread function determination for Keck adaptive optics*, Vol. 9909 of *Adaptive Optics Systems V* (SPIE , 2016), 99091P.

[80] H. Ginis, G. M. Pérez, J. M. Bueno, and P. Artal, Journal of Vision **12**, 20 (2012).

[81] Ximea, MQ013RG-E2 camera, https://www.ximea.com/products/usb-vision-industrial/xiq-usb3-compact-cmos-cameras/e2v-ev76c661-usb3-b-w-nir-compact-camera.

[82] R. S. Jonnal, rjonnal/ciao: initial release – stable and functional, 2020, https://zenodo.org/record/3903941.

[83] W. Zhou, T. W. Raasch, and A. Y. Yi, Applied Optics **55**, 7892 (2016).

[84] Thorlabs, Reflective Neutral Density Filters, https://www.thorlabs.com/newgrouppage9.cfm?objectgroup_id=689.

[85] H. Zhang *et al.*, Biomedical Optics Express **15**, 12345 (2024).

[86] L. Valdivieso-González, A. Muñoz-Potosi, and E. Tepichin-Rodriguez, Optics Communications **454**, 124500 (2020).

[87] W. J. I. Donnelly and R. A. Applegate, Investigative Ophthalmology Visual Science **46**, 3380 (2005).

Appendix

Equations 43, 44 and 45 are related to Zernike polynomials. Equation 43 shows how even (cosine equation) and odd (sine equation) Zernike polynomials are determined. Equation 44 and 45 shows the normalisation factor (N_n^m) and radial polynomial ($R_n^{|m|}$) of the Zernike polynomial. Table V shows the used parameters in Equations 43, 44 and 45. Tables VI and VII show the used components in the aberrometer.

$$Z_j(\rho,\theta) = Z_n^m(\rho,\theta) = \begin{cases} N_n^m R_n^{|m|}(\rho) cos(m\theta), & \text{when } m \geq 0 \\ , N_n^m R_n^{|m|}(\rho) sin(|m|\,\theta) & \text{when } m < 0. \end{cases} \tag{43}$$

$$N_n^m = \sqrt{\frac{2(n+1)}{1+\delta_{m0}}}, \tag{44}$$

$$R_n^{|m|}(\rho) = \sum_{s=0}^{(n-|m|)/2} \frac{(-1)^s (n-s)!}{s!(\frac{n+|m|}{2}-s)!(\frac{n-|m|}{2}-s)!} \rho^{n-2s}, \tag{45}$$

Table V: Parameters and their explanation related to Equations 43, 44 and 45 are shown in this table.

Parameter	Explanation
R_n	Radial polynomial
N_m	Normalization factor
δ_{m0}	Kronecker delta
n	Degree of radial
m	Azimuthal frequency
ρ	Radius of the radial polynomial
s	Index of the sum

Table VI: This table includes every component which are mentioned in Chapter 5.1. The model and manufacturer for every component is shown.

Component	Model	Manufacturer
Light source	Laser diode	Edmund optics, UK
Adapter	SM1FCA2	Thorlabs, USA
Z translation mount	SM1ZA	Thorlabs, USA
Lens tube	SM1L10	Thorlabs, USA
collimator lens	AC127-019-A-ML	Thorlabs, USA
cage system	CP30	Thorlabs, USA
beamsplitter	CP360Q/M	Thorlabs, USA
Lens 1 and 2	AC254-125-B	Thorlabs, USA
aperture	SM1D12CZ	Thorlabs, USA
XY translating lens mount	CXY1A	Thorlabs, USA
cage plate	CP33/M	Thorlabs, USA
mircolens array	MLA150-7AR-M	Thorlabs, USA
CMOS	MQ013RG-E2	Ximea Germany
cage rotation mount	CRM1T/M	Thorlabs, USA

Table VII: These components are needed when measuring the aberrations of the model eyes, as discussed in chapter 5.4. Similarly to table II, this table shows the name of component, model and the manufacturer

Component	Model	Manufacturer
Cage system iris diaphragm	CP20D	Thorlabs, USA
Lens 3	AC-254-100-B	Thorlabs, USA
Aluminum mirror	F10-03	Thorlabs, USA
Kinematic mount	CP35	Thorlabs, USA
Single axis translation stage	PT1	Thorlabs, USA
Pedestal post	RS3P	Thorlabs, USA
post holder	PH2	Thorlabs, USA

The use of artificial intelligence

Artifical intelligence is not used in this master's thesis.